



Hatton, J. E., Hendry, K. R., Hawkings, J. R., Wadham, J. L., Kohler, T. J., Stibal, M., ... Telling, J. (2019). Investigation of subglacial weathering under the Greenland Ice Sheet using silicon isotopes. *Geochimica et Cosmochimica Acta*, 247, 191-206. <https://doi.org/10.1016/j.gca.2018.12.033>

Peer reviewed version

License (if available):
CC BY-NC-ND

Link to published version (if available):
[10.1016/j.gca.2018.12.033](https://doi.org/10.1016/j.gca.2018.12.033)

[Link to publication record in Explore Bristol Research](#)
PDF-document

This is the author accepted manuscript (AAM). The final published version (version of record) is available online via Elsevier at <https://www.sciencedirect.com/science/article/pii/S0016703718307221> . Please refer to any applicable terms of use of the publisher.

University of Bristol - Explore Bristol Research

General rights

This document is made available in accordance with publisher policies. Please cite only the published version using the reference above. Full terms of use are available:
<http://www.bristol.ac.uk/pure/about/ebr-terms>

1 Investigation of subglacial weathering under the Greenland Ice Sheet using 2 silicon isotopes.

3 J. E. Hatton^{1*}, K. R. Hendry¹, J. R. Hawkings^{2,3,4}, J. L. Wadham², T. J. Kohler^{5,6}, M. Stibal⁵, A. D.
4 Beaton⁷, E. A. Bagshaw⁸, J. Telling⁹

5 ¹School of Earth Sciences, University of Bristol. (*correspondence: j.e.hatton@bristol.ac.uk)

6 ²School of Geographical Sciences, University of Bristol.

7 ³National High Magnetic Field Lab and Earth, Ocean and Atmospheric Sciences, Florida State
8 University, USA

9 ⁴German Research Centre for Geosciences GFZ, Potsdam, Germany

10 ⁵Department of Ecology, Faculty of Science, Charles University.

11 ⁶Stream Biofilm and Ecosystem Research Laboratory, School of Architecture, Civil and Environmental
12 Engineering, École Polytechnique Fédérale de Lausanne, CH-1015 Lausanne, Switzerland.

13 ⁷Technology and Engineering Group, National Oceanography Centre, Southampton.

14 ⁸School of Earth and Ocean Sciences, Cardiff University.

15 ⁹School of Natural and Environmental Sciences, Newcastle University.

16

17 *Jade E Hatton, Bristol Glaciology Centre, School of Geographical Sciences, University of Bristol,
18 University Road, BS8 1SS, UK (jh12528@bristol.ac.uk)

19 Katharine R Hendry, School of Earth Sciences, University of Bristol, Bristol, BS8 1RJ, UK
20 (k.hendry@bristol.ac.uk)

21 Jon R Hawkings, National High Magnetic Field Lab and Earth, Ocean and Atmospheric Sciences,
22 Florida State University, Tallahassee, Florida, USA (jhawkings@fsu.edu); German Research Centre
23 for Geosciences GFZ, Telegrafenberg, Building C, 14473, Potsdam, Germany ([hawkings@gfz-
potsdam.de](mailto:hawkings@gfz-
24 potsdam.de))

25 Jemma L Wadham, Bristol Glaciology Centre, School of Geographical Sciences, University of
26 Bristol, University Road, BS8 1SS, UK (j.l.wadham@bristol.ac.uk)

27 Tyler J Kohler, Stream Biofilm and Ecosystem Research Laboratory, School of Architecture, Civil and
28 Environmental Engineering, École Polytechnique Fédérale de Lausanne, CH-1015 Lausanne,
29 Switzerland (tyler.j.kohler@gmail.com)

30 Marek Stibal, Faculty of Science, Department of Ecology, Charles University, Viničná 7, 12844
31 Prague 2, Prague, Czech Republic (marek.stibal@natur.cuni.cz)

32 Alexander Beaton, National Oceanography Centre Southampton, Waterfront Campus, European Way,
33 Southampton, SO14 3ZH, UK (a.beaton@noc.ac.uk)

34 Elizabeth Bagshaw, School of Earth and Ocean Sciences, Cardiff University, Main Building, Park
35 Place, Cardiff, CF10 3AT, UK (bagshawe@cardiff.ac.uk)

36 Jon Telling, School of Natural and Environmental Sciences, Newcastle University, NE1 7RU, UK
37 (jon.telling@newcastle.ac.uk)

38

39 Abstract

40 **Subglacial chemical weathering plays a key role in global silicate weathering budgets,**
41 **contributing to the cycling of silicon (Si) in terrestrial and marine systems and the potential**
42 **drawdown of carbon dioxide from the atmosphere. Here, we use data from two Greenland Ice**
43 **Sheet (GrIS) catchments to demonstrate how Si isotopes from dissolved and amorphous**
44 **particulate fractions ($\delta^{30}\text{DSi}$ and $\delta^{30}\text{ASi}$ respectively) can be used together with major ion data**
45 **to assess the degree of secondary silicate weathering product formation and redissolution in**
46 **subglacial environments. We compare a time-series of summer melt seasons from the two study**
47 **sites, which differ in catchment size (~600 km² for Leverett Glacier (LG) and ~36 km² for**
48 **Kiattuut Sermiat (KS)). Subglacial waters from LG have elevated Na⁺ and K⁺ ions in relation to**

49 **Ca²⁺ and Mg²⁺ ions, indicating a predominance of silicate weathering, whilst meltwaters from**
50 **KS are characterised by carbonate weathering (hydrolysis and carbonation) throughout the**
51 **melt season. Both catchments have mean $\delta^{30}\text{DSi}$ values substantially lower than average riverine**
52 **values (KS 0.41‰, LG -0.25‰, versus a global riverine mean of 1.25‰) and display a seasonal**
53 **decline, which is more pronounced at LG. The $\delta^{30}\text{ASi}$ values (discharge weighted mean values**
54 **KS -0.44‰, LG -0.22‰) are lighter than the bedrock (mean values KS $-0.18\pm 0.12\%$, LG**
55 **$0.00\pm 0.07\%$) in both catchments, indicating a secondary weathering product origin or leaching**
56 **of lighter isotopes during initial weathering of crushed rock. When used in combination, the**
57 **major ion and silicon isotope data reveal that the extent of silicate weathering and secondary**
58 **phase redissolution are more pronounced at LG compared to KS. Contrasting weathering**
59 **regimes and subglacial hydrology between catchments need to be considered when estimating**
60 **the $\delta^{30}\text{Si}$ composition of silica exported into polar oceans from the GrIS, with larger catchments**
61 **likely to produce fluxes of lighter $\delta^{30}\text{Si}$. As larger catchments dominate freshwater export to the**
62 **ocean, GrIS meltwater is likely to be very light in isotopic composition, and the flux is likely to**
63 **increase with ice melt as the climate warms.**

64

65 **1. Introduction**

66 The weathering of silicate minerals plays an important role in biogeochemical cycles, producing
67 dissolved silicate (DSi) and dissolvable amorphous silica (ASi) into terrestrial and marine systems,
68 whilst consuming carbon dioxide (CO₂) (Walker et al., 1981; Berner, 2003). DSi is generated through
69 physical weathering and the subsequent chemical dissolution of silicate minerals, and then mobilised
70 via fluvial hydrological systems. Primary weathering processes also lead to secondary mineral
71 formation. Secondary weathering products, such as clays and ASi have varying solubility and may
72 contribute DSi to the fluvial system through redissolution processes (Frings et al., 2016). The resultant
73 DSi is converted to biogenic silica (BSi) by siliceous organisms, including diatoms, which are
74 responsible for 35-70% of oceanic productivity (Nelson et al., 1995). Weathering processes,
75 precipitation, and biogenic uptake result in fractionation of silicon isotopes, meaning isotopic analysis
76 can provide insight into the weathering regimes and biological utilisation of Si within aquatic systems
77 (De la Rocha et al., 1997; De La Rocha et al., 2000; Fontorbe et al., 2013; Frings et al., 2016).

78 Glaciation promotes physical and chemical weathering, with dynamic hydrological and microbial
79 systems upon, within and beneath ice (Wadham et al., 2010; Tranter and Wadham, 2014). It is likely
80 that weathering beneath large ice sheets is silicate mineral dominated (Stevenson et al., 2017), due to
81 the enhanced residence times of subglacially stored waters, which result in exhaustion of carbonate
82 minerals or saturation of meltwaters with respect to calcite (Wadham et al., 2010; Hindshaw et al.,
83 2014; Michaud et al., 2016). This is evidenced by the ionic composition of meltwaters (high relative

84 proportions of Na⁺ and K⁺) from the bed of the Greenland Ice Sheet (GrIS) (Graly et al., 2014) and the
85 Antarctic Ice Sheet (AIS) (Michaud et al., 2016) compared to Alpine valley glaciers. Recently, there
86 has been increased focus on the chemical composition of GrIS meltwaters in an attempt to improve
87 the understanding of weathering processes in large ice sheet catchments and associated nutrient
88 release (Graly et al., 2014; Hindshaw et al., 2014; Yde et al., 2014; Graly et al., 2017; Kohler et al.,
89 2017). High fluxes of Si resulting from weathering processes have been reported from ice sheets. For
90 example, Hawkings et al. (2017) estimated silica fluxes from GrIS to be approximately 50% of input
91 from Arctic rivers (0.20 Tmol year⁻¹). However, the mechanisms and control on silicate dissolution
92 processes in ice sheet catchments are currently poorly understood, which is compounded by the
93 difficulty of acquiring data over an entire melt season and across differing hydrological regimes in
94 challenging environments. An improved understanding of the complex nature and extent of subglacial
95 silicate weathering is necessary to fully understand and quantify silicon cycling on a global scale
96 (Graly et al., 2014; Hindshaw et al., 2014; Yde et al., 2014).

97 Silicon isotopes (denoted by $\delta^{30}\text{Si}$) are increasingly used as a tool for studying continental weathering
98 (Ding et al., 2004; Georg et al., 2007; Opfergelt et al., 2013; Chemtob et al., 2015), especially in
99 riverine systems (Ding et al., 2004; Cardinal et al., 2010; Ding et al., 2011; Fontorbe et al., 2013;
100 Frings et al., 2016). Silicon has three stable isotopes; ²⁸Si, ²⁹Si and ³⁰Si with relative abundances of
101 92.2%, 4.7% and 3.1% respectively (Ding et al., 2005). The isotopic composition is reported relative
102 to international reference standard NBS-28, as a deviation from the ratio of ²⁸Si/³⁰Si of the sample
103 from the reference standard (Equation 1, Frings et al. 2016). The isotopic composition of the lower
104 crust (-0.29±0.04‰), middle crust (-0.23±0.04‰) and bulk earth values (-0.29±0.08‰) are well
105 characterised (Savage et al., 2010; Savage et al., 2013). Relatively large fractionation occurs during
106 weathering processes as newly formed secondary weathering products are enriched with lighter
107 isotopes (Andre et al., 2006; Frings et al., 2016). The range of DSi isotopic compositions in rivers
108 draining from non-glaciated catchments is currently 0.4-3.4‰ (De La Rocha et al., 2000; Ding et al.,
109 2004; Cardinal et al., 2010; Ding et al., 2011), with a global mean of 1.25±0.68‰ (Frings et al., 2016).
110 Riverine DSi is therefore generally enriched in the ³⁰Si isotope compared with bulk silicate earth and
111 suspended particulate matter, which is isotopically lighter on average (-0.18‰, Frings et al., 2016;
112 Ding et al. 2004). Precipitated silica from the formation of secondary weathering or biological uptake
113 is enriched in ²⁸Si, due to preferential uptake of the lighter isotope, resulting in an enrichment of ³⁰Si
114 in the dissolved phase (De la Rocha et al., 1997; De La Rocha et al., 2000; Ziegler et al., 2002; Ding
115 et al., 2004). However, whilst these generalisations about the fractionation of low temperature
116 processes can be made, more definite fractionation factors for many environmental processes are still
117 very uncertain (Frings et al., 2016).

118 Studies of Icelandic rivers have shown that catchments with greater glacial coverage have a lighter
119 dissolved $\delta^{30}\text{Si}$ composition ($\delta^{30}\text{DSi}$) compared to non-glacial rivers (Georg et al., 2007). Opfergelt et

120 al. (2013) reported glacial rivers to have a mean composition of $0.17 \pm 0.18\text{‰}$ compared to $0.97 \pm$
121 0.31‰ for non-glacial rivers. The dissolved phase exported from a large ice sheet catchment of GrIS
122 has also been shown to have an isotopic composition lighter than the bulk bedrock ($-0.25 \pm 0.12\text{‰}$
123 compared to $0.00 \pm 0.07\text{‰}$, Hawkings et al., 2018). These studies indicate that subglacial processes
124 could be influencing the isotopic composition of meltwaters. Si isotope systematics could potentially
125 be used to provide insight into silicate dissolution and redissolution of secondary weathering products
126 within the subglacial environment. However, we currently lack high resolution time series data to
127 show whether these patterns are consistent across glacial catchments and to explain the mechanism
128 driving the export of low $\delta^{30}\text{Si}$. We need to gain a better understanding of subglacial biogeochemical
129 processes, and their impact on the $\delta^{30}\text{Si}$ compositions of exported dissolved and particulate phases.
130 This will allow us to quantify the impact of Si exported from GrIS on the wider silica cycle and make
131 predictions about how export from large ice sheets may change over longer timescales.

132 Here we combine new $\delta^{30}\text{Si}$ measurements of DSi and ASi phases with hydrogeochemical data from
133 GrIS glacial catchments of contrasting scale over the summer melt season, in order to improve the
134 current understanding of subglacial weathering processes.

135 **2. Methodology**

136 **2.1 Sampling locations**

137 We present hydrological and geochemical data from two polythermal- based, land terminating outlet
138 glaciers from the GrIS, both of which have subglacial drainage systems that develop seasonally
139 (Bartholomew et al., 2011). Data were collected from the proglacial river exiting Kiattuut Sermiat
140 (KS; 61.2°N , 45.3°W ; Fig. 1) from April to August 2013 and Leverett Glacier, (LG; 67.06°N ,
141 50.17°W ; Fig. 1) from May to July 2015 to capture the composition of meltwaters exiting the glaciers
142 during the summer ablation season. KS is a small coastal glacier, covering an area of 36km^2 and
143 currently terminating in a proglacial lake of approximately 0.5km^2 (Hawkings et al., 2016; Dubnick et
144 al., 2017). Calculations using discharge records find the turnover time of the proglacial lake to be
145 relatively short once the glacial melt season begins (less than 24 hours from Day 157, Supplementary
146 Fig. 1), indicating that the lake will likely not have a significant effect on the meltwater chemistry
147 downstream. In comparison, LG is a much larger glacier, with a hydrologically active catchment of
148 around 600km^2 (Cowton et al., 2012), which feeds into Watson River and then into the Davis Strait
149 via the Søndre Strømfjord (Hawkings et al., 2016). The composition of bedrock beneath LG is
150 dominated by Precambrian Shield crystalline gneiss and granite, which is representative of the
151 majority of GrIS (Escher, 1976) and much of the bedrock that was covered by the Eurasian and North
152 American Ice Sheets (Bouysse, 2014). The bedrock at KS is relatively similar to LG, but there are
153 some potential differences. KS overlays the Gardar Province, containing basalts, trachytes and
154 phonolites. This region may also include syenites from the intrusive rocks of the Julianhåb batholith

155 (Henriksen, 2009). However, previous work on $\delta^{30}\text{Si}$ fractionation and elemental differentiation
156 during high temperature processes in the mantle has shown limited isotope fractionation in
157 comparison to weathering and biological processes (Savage et al., 2010).

158 We carried out hydrological monitoring of discharge, suspended sediment, pH and electrical
159 conductivity using *in-situ* hydrochemical sensors (Fig. 1), as detailed by Kohler et al. (2017) and
160 Hawkings et al. (2018). Water samples were collected at least once a day from just below the surface
161 of the proglacial river using 1L Nalgene™ bottles (HDPE). Samples were filtered immediately using
162 0.45 μm cellulose nitrate membrane filters (Whatman®) mounted on a PS filtration stack (Nalgene™)
163 and kept refrigerated in the dark until laboratory analysis. Samples for ASi concentrations and
164 amorphous isotopic composition ($\delta^{30}\text{ASi}$) were collected by filtering approximately 500ml of the
165 same water sample collected for dissolved analysis through a 0.45 μm cellulose nitrate membrane
166 filters (Whatman®), retaining the sediment. Filters were kept refrigerated and in the dark until being
167 gently air dried under a laminar flow hood prior to laboratory analysis.

168

169 **2.2 Major Ion Composition**

170 Water samples were analysed for major cation (Na^+ , K^+ , Ca^{2+} and Mg^{2+}) and anion (NO_3^- , SO_4^{2-} and
171 Cl^-) concentrations by ion chromatography, with HCO_3^- estimated using the charge deficit (Tranter et
172 al., 2002). Measurements were carried out using a Thermo Scientific™ Dionex™ capillary ICS-5000
173 fitted with anion and cation columns (Hawkings et al., 2015; Dubnick et al., 2017).

174

175 **2.3 Silica concentrations**

176 DSi concentrations were determined spectrophotometrically using Flow Injection Analysis (FIA) on a
177 LaChat 8500 series (QuikChem Method 31-114-27-1-D), as outlined by Hawkings et al. (2017). The
178 limit of detection was 0.3 μM . Precision and accuracy ($\pm 0.54\%$ and $\pm 1.9\%$) were determined by repeat
179 measurements of a gravimetrically weighed 8.9 μM standard (n=17). ASi was determined using an
180 alkaline extraction method adapted from DeMaster (1981), as used by Hawkings et al. (2017). ASi
181 was extracted from the suspended sediments collected on 0.45 μm filters in the field. Briefly, 50ml
182 0.1M Na_2CO_3 was added to ~30mg (accurately weighed) of sediment at 85°C with 1ml aliquots taken
183 at 2, 3 and 5 hours. Aliquots were neutralised immediately with 0.021M HCl and stored at 4°C until
184 FIA analysis, using the same method as DSi concentrations. ASi (wt%) was calculated following
185 DeMaster (1981). Na_2CO_3 was preferred over NaOH extractions as it is the most commonly used
186 alkaline extraction method of aquatic sediments, and is calibrated to clay minerals (Conley, 1998;
187 Sauer et al., 2006; Hawkings et al., 2017). However, a 0.2M NaOH extraction method was required to
188 extract the total reactive silica for silicon isotope analysis and both methods have been compared to
189 ensure consistency between the ASi concentrations reported and the ASi extracted for silicon isotope
190 analysis. The NaOH extraction produced similar or slightly lower concentrations compared to the

191 Na₂CO₃ method (Hawkings et al., 2018). Saturation indices for ASi were calculated for each
192 timepoint using hydrochemical data from KS and LG and Debye-Hückel ion interaction model in
193 Geochemists Workbench® Student Edition.

194

195 **2.4 Silicon Isotope Composition**

196 All silicon isotope analysis was completed in the Bristol Isotope Group laboratories (University of
197 Bristol) using a Thermo Scientific™ Neptune Plus™ High Resolution MC-ICP-MS and a standard-
198 sample-standard bracketing procedure with Mg doping (100µl 10ppm Mg) to correct for mass bias
199 (Cardinal et al., 2003; Hendry and Robinson, 2012). International reference standard NBS-28 (NIST
200 RM8546, purified quartz sand) was used as the bracketing standard and isotope compositions are
201 reported in terms of δ³⁰Si (Equation 1). Samples were doped with 50-100µL 0.1M sulphuric acid
202 (Romil-UpA) to ensure matrix match between sample and standard, to reduce the mass bias effects of
203 anion loading (Hughes et al., 2011). Instrument blanks were <1% of ²⁸Si signal and typical internal
204 reproducibility was ±0.08‰ for δ³⁰Si (2SD) and ±0.04‰ for δ²⁹Si (2SD). Long term reproducibility
205 of reference standards Diatomite and LMG08 (sponge) are reported as +1.22 ±0.15‰ and -3.45
206 ±0.14‰ (2SD) respectively. Mass dependent fractionation is demonstrated by a three-isotope plot of
207 all samples analysed during the study (Supplementary Fig. 2) with a gradient of 0.5118 (Reynolds et
208 al., 2007).

209

210 Sediment samples for δ³⁰ASi composition were prepared by adding 1ml 0.2M NaOH per 0.1mg ASi
211 and heating at 100°C for 1 hour. Samples were diluted and acidified with 8N HNO₃ and filtered
212 through 0.22µm PES syringe filters. Bulk bedrock samples were processed using alkaline fusion
213 (Georg et al., 2006) and the full procedure is detailed in Hawkings et al. (2018). Briefly, coarse,
214 unsorted debris were crushed and ground to form a fine powder using a planetary ball mill (Fritsch
215 Planetary Mono Mill Pulverisette 6). Debris was collected in front of the portal at LG and an ice cave
216 into the front of KS. Samples were then furnace at 730°C with a NaOH pellet (approximately
217 200mg), diluted with MQ and acidified with 8N HNO₃ once cool. Water samples were prepared for
218 δ³⁰DSi by preconcentrating the samples via evaporation to approximately 2ml sample, ensuring 2ppm
219 of Si for analysis. All samples were then added to pre-cleaned BioRad exchange resin (AG50W-X12)
220 columns and eluted with MQ water (Georg et al., 2006).

221

222 **3. Results**

223 **3.1 Defining periods of the melt seasons at KS and LG**

224 We categorise the melt season into three parts at KS, following Dubnick et al. (2017); Early Season,
225 Transition Period and Late Season. These categories are defined by distinct changes in the proglacial
226 river hydrochemistry. The Early Season is defined by low discharge and a lack of relationship

227 between solutes, which is unlikely to reflect a subglacial signal. The Transition Period likely reflects
228 the time when the subglacial system became hydrologically connected and the bulk meltwaters
229 included a subglacially stored contribution (Hawkings et al., 2016; Dubnick et al., 2017). This period
230 includes a “Spring Event”, which is a time of high glacier velocity, associated with increases in
231 subglacial water pressure discharge, suspended sediment and the divalent to monovalent cation ratio
232 (Dubnick et al., 2017, Mair et al., 2004; Fig. 2). The Late Season had a bulk melt water signature that
233 was distinct from the other periods analysed and is more similar to Alpine glacier geochemistry
234 (Tranter et al., 2002, Tranter and Wadham., 2014).

235 We also categorise the melt season at LG into Early Season and Late Season, defined by differences
236 in the hydrochemical data, with the transition being the first outburst event of the melt season. After
237 this outburst event, the hydrochemistry of the meltwaters shifts towards those indicative of silicate
238 mineral dissolution, as longer residence time waters are flushed.

239 **3.2 Dissolved major ions, DSi and $\delta^{30}\text{DSi}$**

240 The ratio of $(\text{Ca}^{2+} + \text{Mg}^{2+})$ to $(\text{Na}^{+} + \text{K}^{+})$ (divalent to monovalent cations, reported hereafter as D:M) has
241 traditionally been used to indicate the amount of silicate weathering in relation to carbonate
242 weathering (Tranter et al., 2002; Wadham et al., 2010). Elevated monovalent ion concentrations in
243 relation to divalent concentrations are associated with enhanced silicate mineral weathering. The
244 dissolved ion composition of glacial runoff from the two catchments changed significantly with
245 seasonal evolution of the subglacial drainage system (Fig. 3). The discharge-weighted mean (Qwt)
246 D:M ($\mu\text{eq L}^{-1} : \mu\text{eq L}^{-1}$) at LG was 1.36 compared to 6.91 at KS, with the D:M decreasing at LG as the
247 melt season progressed, from 5.18 to 1.44, compared to an increase in the D:M of a smaller magnitude
248 at KS (6.57 to 7.72, Fig. 3). Ca^{2+} was the dominant cation in KS over the entire melt season, consistent
249 with previously documented meltwaters from Alpine and Polar glaciers. However, there was a shift
250 from Ca^{2+} to Na^{+} as the dominant cation as the melt season progressed at LG (Ca/Na molar ratios
251 started at 3.23 and decreased to 0.56 during outburst events, Fig. 4).

252 DSi concentrations in LG meltwaters decreased as the season progressed due to dilution from
253 supraglacial meltwaters ($56.9\mu\text{M}$ to $9.21\mu\text{M}$). The discharge weighted mean DSi concentration was
254 $20.8\mu\text{M}$, similar to previously reported concentrations (Hindshaw et al., 2014; Hawkings et al., 2017).
255 KS had a slightly higher discharge weighted mean DSi of $22.2\mu\text{M}$, with a range of $14.8\mu\text{M}$ to 41.8
256 μM . Concentrations also decreased as the subglacial hydrological drainage system developed from
257 inefficient to efficient drainage pathways (Supplementary Table 3 and 4).

258 There was a substantial decline in $\delta^{30}\text{DSi}$ at LG as the melt season progressed and the subglacial
259 system became hydrologically connected, with drainage of more isolated regions of the bed further up
260 catchment (Fig. 5d). The discharge weighted mean value of $\delta^{30}\text{DSi}$ at LG ($-0.25 \pm 0.12\text{‰}$) was lighter
261 than the previous riverine average $\delta^{30}\text{DSi}$ composition ($+1.25\text{‰}$, Frings et al., 2016), and studies of

262 glacially fed rivers in Iceland ($+0.17 \pm 0.18\%$, Opfergelt et al., 2013). The lightest values measured at
263 LG are more comparable to long residence time groundwaters (up to -1.42% , Georg et al., 2009). KS
264 had a higher $\delta^{30}\text{DSi}$, with a discharge weighted mean of $+0.41 \pm 0.10\%$, although this value is also
265 below the average riverine silicon isotope composition (Frings et al., 2016). The $\delta^{30}\text{DSi}$ at KS also
266 declined after the connection of the subglacial hydrological system (“Spring Event”, Hawkings et al.,
267 2016, Mair et al. 2004) but the decline was not as substantial as that seen at LG (Fig. 5c).

268 **3.3 Saturation Indices**

269 Bulk meltwaters in both catchments were highly undersaturated with respect to ASi throughout the
270 melt season (LG $\text{SI}_{\text{ASi}} = -1.04$ to -1.85 and KS $\text{SI}_{\text{ASi}} = -1.12$ to -1.73). The lightest $\delta^{30}\text{DSi}$ composition
271 occurred when the proglacial river was most undersaturated with respect to ASi at both catchments
272 (Supplementary Fig. 3).

273 **3.4 Bedrock, SPM, ASi concentration and $\delta^{30}\text{ASi}$.**

274 Suspended particulate matter (SPM) concentrations in bulk meltwaters generally increased over time
275 in both catchments, as increasing amounts of sediment were entrained subglacially (Fig. 2). LG ASi
276 and SPM concentrations were significantly higher than KS (Table 1), with peak SPM coinciding with
277 subglacial outburst events (Hawkings et al. 2016, Fig. 2). Particles at LG also had a higher relative
278 proportion of extractable ASi, contributing to the elevated ASi concentrations (LG Qwt mean =
279 $0.73\text{wt}\%$, compared to KS Qwt mean = $0.23\text{wt}\%$). However, KS has a higher specific discharge than
280 LG, so the yield of Si per km^2 is higher at KS. We estimate a mean annual ASi yield of $1.75 \times 10^4 \text{ kg}$
281 km^{-2} from KS (Day 128 - 221) compared to an estimated mean yield of $1.24 \times 10^4 \text{ kg km}^{-2}$ from LG
282 (Day 135 – 210).

283 The $\delta^{30}\text{ASi}$ composition of SPM in bulk runoff was lighter at KS compared to LG, with little variation
284 at either site over the monitoring period (discharge weighted mean of $-0.47 \pm 0.06\%$ compared to -
285 $0.22 \pm 0.06\%$, Fig. 5). These values were lower than the local bedrock (KS $-0.18 \pm 0.06\%$, LG $0.00 \pm$
286 0.07%) and bulk suspended sediment (KS $-0.32 \pm 0.12\%$, LG $-0.09 \pm 0.07\%$).

287 **4. Discussion**

288 **4.1 Conceptual model of subglacial hydrology**

289 Differences in drainage system characteristics of glaciers at different spatial scale may result in
290 contrasting chemical weathering environments and water export mechanisms (Wadham et al., 2010;
291 Graly et al., 2014). Subglacial drainage systems of GrIS catchments likely include hydrological
292 elements that exist for the majority of the year and those that develop over time and shut down during
293 winter (Dubnick et al., 2017). The progression of the melt season is accompanied by an evolution
294 from slow-inefficient distributed to efficient (and potentially channelised) drainage systems as more

295 supraglacial meltwater reaches the bed (Bartholomew et al., 2011). Previous studies have
296 demonstrated that the seasonal evolution of subglacial hydrology impacts nutrient export dynamics
297 via the connection of chemically distinct, solute sources at the glacier bed (Bartholomew et al., 2011;
298 Bhatia et al., 2013; Hawkings et al., 2016; Dubnick et al., 2017; Kohler et al., 2017). LG has a
299 hydrologically active catchment of $\sim 600\text{km}^2$, is 80km long and has inland ice of low topography,
300 favouring the formation of large supraglacial lakes (often \sim kms in diameter, Hoffman et al., 2011).
301 These supraglacial lakes can drain rapidly (<2 hours) through moulins to the glacier bed as a result of
302 hydrofracturing (Das et al., 2008; Bartholomew et al., 2011). Such drainage events can result in
303 outburst events being recorded in the proglacial hydrochemical records (Bartholomew et al., 2011;
304 Hawkings et al., 2015). Proglacial river discharge, suspended sediment and electrical conductivity
305 rapidly rise (Bartholomew et al., 2011, Hawkings et al., 2016; Fig. 2), as subglacially stored waters
306 and sediment become hydrologically connected and flushed downstream by incoming supraglacial
307 water (Bartholomew et al., 2011; Cowton et al., 2012; Chandler et al., 2013). Subglacial hydrological
308 evolution from inefficient to efficient drainage at the bed progresses from marginal to inland locations,
309 with artificial tracer work showing efficient drainage existing up to 40km from the margin by late July
310 (Chandler et al., 2013). This evolution is further supported by the seasonal progression of the ^{14}C age
311 of exported POC at LG (Kohler et al., 2017). The inland progression of the subglacial system could
312 mean that increasingly isolated meltwaters drain from the bed, since the interval between basal
313 flushing events via supraglacial lake drainage or moulins is longer in more inland locations
314 (potentially 10 months) compared to marginal locations (Harper and Humphrey, 1995). Residence
315 time differences between marginal and the most isolated inland waters are therefore likely to exist,
316 especially if similar regions of the bed are flushed annually (Fig. 6), with implications for weathering
317 and redissolution processes.

318 KS is only $\sim 16\text{km}$ in length and there is comparatively little altitudinal difference from snout to the
319 top of the ablation area. Supraglacial lakes do not form at KS, thus some more isolated parts of the
320 bed may not be annually flushed by surface-to-bed water flow. The subglacial drainage system
321 development at KS is driven entirely by the progression of the snowline and the consequent opening
322 of new moulins and crevasses for surface to bed water flow, similar to smaller Arctic and Alpine
323 glaciers. Thus, the subglacial drainage system develops from inefficient distributed drainage, where
324 water follows a tortuous flow path, to an efficient, channelised system as the ablation season
325 progresses and meltwater inputs increase (Fig. 6, Tranter et al., 2002, Nienow et al., 2014). The
326 absence of supraglacial lake drainage and the smaller catchment size will shorten average residence
327 times of water emerging as bulk runoff. Any seasonal variation in subglacial water residence times is
328 likely on the order of weeks rather than months. We propose that the full length of KS could be
329 compared with the evolution of the first 10-20km of subglacial hydrology at LG prior to the onset of
330 outburst events, as demonstrated by the relationship between discharge and $\delta^{30}\text{DSi}$ (Fig. 5b). As there

331 is a limited input of long residence time stored water with differing geochemical composition at KS,
332 the chemical composition of the proglacial stream reflects a carbonate dominated weathering regime
333 (Tranter et al., 2002).

334 **4.2 Differences in weathering regimes**

335 Glacier size is hypothesised to have a major impact on chemical weathering via its influence upon
336 hydrological flow path length, and hence water residence times (Wadham et al., 2010). Our data show
337 clear differences in the major ion composition of bulk meltwaters draining from the study glacial
338 catchments (Figs. 3 and 7), indicating contrasting subglacial chemical weathering regimes. In larger
339 catchments silicate mineral dissolution is enhanced, as subglacially stored meltwaters reach saturation
340 with respect to calcite, due to the long residence times and subglacial isolation (Wadham et al., 2010;
341 Hawkings et al., 2016). Carbonate hydrolysis was previously believed to dominate over carbonation
342 in subglacial environments, due to the limited atmospheric connectivity, resulting in enhanced
343 concentration of divalent ions in meltwaters ($\text{Ca}^{2+} + \text{Mg}^{2+}$; Equation 2, Tranter et al., 2002). By
344 comparison, silicate hydrolysis results in elevated concentrations of monovalent ions ($\text{K}^+ + \text{Na}^+$;
345 Equation 3, Tranter and Wadham, 2014).

346 Leverett Glacier

347 At LG, the progressive evolution in the D:M ratio is consistent with a shift towards silicate dominated
348 mineral weathering as the melt season progresses (Fig. 3). This trend in D:M is also consistent with
349 the Na-normalised molar ratios, which can be used to compare the hydrochemical signature to silicate
350 and carbonate endmembers in mixing diagrams (Gaillardet et al., 1999). Fig. 4 shows the evolution of
351 the LG towards the silicate endmember as the melt season progresses, with the outburst events lying
352 closest to this endmember. This suggests that isolated meltwaters characterised by long residence
353 times become hydrologically connected to a fast, efficient drainage systems and are exported to the
354 ice margin.

355 Subglacial meltwaters in inland regions may only be flushed by surface melt (e.g. via lake drainage
356 and moulins) after ~10 months when the snowline retreats this far from the ice margin and inland
357 hydrological systems become connected. During the intervening period, these subglacial meltwaters
358 are inferred to undergo enhanced silicate dissolution (Wadham et al., 2010; Chandler et al., 2013;
359 Graly et al., 2014). Hydrolysis of silicates also increases the pH within subglacial waters (Equations 2
360 and 3, Fig. 2), and these higher pH conditions further enhance the dissolution of aluminosilicate
361 minerals (Georg et al., 2009; Tranter and Wadham, 2014). Evolution towards low D:M ratios, and
362 elevated pH is particularly pronounced from Day 170 onwards in 2015 at LG after the first subglacial
363 outburst event (Q_{wt} pH after first outburst event 8.71, Fig. 2).

364 Coupled carbonate dissolution and sulphide oxidation is a more important process, during the Early
365 Season at LG. This importance is illustrated by gradients of $\text{Ca}^{2+}+\text{Mg}^{2+}$ versus SO_4^{2-} (Fig. 7a) and of
366 $\text{Ca}^{2+}+\text{Mg}^{2+}$ versus HCO_3^- (Fig. 7b) close to 2 (1.93 and 1.50 respectively, Tranter et al., 2002), which
367 closely resemble molar equivalent ratios of 2:1 for $\text{Ca}^{2+}+\text{Mg}^{2+}$ and SO_4^{2-} , and $\text{Ca}^{2+}+\text{Mg}^{2+}$ and HCO_3^- ,
368 according to Equation 5. These findings are similar to those found by Graly et al. (2017), but are not
369 seen in a study which focused upon the middle to late part of the melt season at LG (Hindshaw et al.,
370 2014). We find higher concentrations of SO_4^{2-} in 2015 during the Early Season when discharge was
371 lower (Supplementary Fig. 4), which we can attribute to sulphide oxidation, highlighting the
372 importance of categorising the development of the melt season due to potentially large seasonal
373 differences. Furthermore, during the Early Season, the sulphate mass fraction (SMF, Equation 6) is
374 higher than later in the season (Supplementary Fig. 5), indicating a larger proportion of protons result
375 from sulphide oxidation. However, a SMF of <0.5 throughout the melt season indicates carbonation is
376 overall more important than sulphide oxidation as a proton supplier.

377 Following the first outburst event (Late Season), the gradients of $\text{Ca}^{2+}+\text{Mg}^{2+}$ v SO_4^{2-} and $\text{Ca}^{2+}+\text{Mg}^{2+}$
378 v HCO_3^- became shallower ($\text{Ca}^{2+}+\text{Mg}^{2+}:\text{SO}_4^{2-} = 1.50:1$, $\text{Ca}^{2+}+\text{Mg}^{2+}:\text{HCO}_3^- = 0.79:1$). The SMF also
379 decreases (~ 0.45 to ~ 0.25), indicating protons are largely provided from carbonation reactions. It is
380 likely that silicate dissolution via hydrolysis and carbonation is occurring in the Late Season at LG
381 (Wadham et al., 2010), especially when considering the concomitant increase in the gradient of the
382 lines of best fit for associations between HCO_3^- and SO_4^{2-} (Fig. 7c and embedded Table) from Early to
383 Late season at LG (0.96 to 1.17). Carbonation of silicates and carbonates consumes CO_2 in solution
384 and result in formation of HCO_3^- , which, combined with silicate hydrolysis, also helps to explain the
385 increasing pH as the melt season progresses. We expect that this increase in pH is the result of
386 increased hydrolysis and carbonation of silicates, due to the decline of $\text{Ca}^{2+}+\text{Mg}^{2+}:\text{HCO}_3^-$ ratios as the
387 season progresses, indicating that the addition of HCO_3^- is occurring in the absence of $\text{Ca}^{2+}+\text{Mg}^{2+}$.

388 The meltwater geochemistry therefore suggests that LG begins as a system with the imprint of
389 sulphide oxidation coupled to carbonate dissolution (SMF = ~ 0.45 , Equation 5). As the season
390 progresses and more isolated waters are exported, there is an increased importance of silicate
391 weathering linked to carbonation reactions (SMF = ~ 0.2).

392 Kiattuut Sermiat

393 Our conceptual model of the hydrology at KS leads to predictions of a relatively consistent subglacial
394 weathering regime once an efficient drainage system has developed. The source of solute in the
395 meltwaters at KS appears fairly consistent over the melt season. D:M ratio and mixing diagrams at KS
396 indicates that the system is dominated by carbonate weathering (Figs. 3, 4; also see Dubnick et al.
397 2017). We can use the ionic ratios to interrogate these relationships further and assess differences
398 between Early Season, Transition Period and Late Season.

399 During the Early Season at KS there is no significant relationships between $\text{Ca}^{2+}+\text{Mg}^{2+}$ and HCO_3^-
400 versus SO_4^{2-} . We would expect the higher SO_4^{2-} concentrations to be a result of sulphide oxidation.
401 Sulphide oxidation would usually be coupled with carbonate dissolution in glacial systems, which
402 should be reflected in molar equivalent ratios (Equation 5). However, the discharge is low at this time,
403 so it is likely that the proglacial river reflects groundwaters diluted with some snowmelt and/or
404 precipitation. Groundwater flow may be torturous, impacting upon the ionic ratios, and it is also likely
405 that these waters are more affected by atmospheric deposition than later in the season when discharge
406 is much greater (Bhatia et al., 2013). In the Early Season there are also longer turnover times of lake
407 water due to the lower discharge entering the lake, which results in slower flushing of system
408 (Supplementary Fig. 1).

409 It is during the Transition Period that the gradients for all the major ion relationships most closely
410 match those during the Early Season at LG (Fig. 7). There was an increase of HCO_3^- and $\text{Ca}^{2+}+\text{Mg}^{2+}$
411 in relation to SO_4^{2-} (Fig. 7a and 7c), which could be evidence of the connection of the subglacial
412 system to the proglacial hydrological system. As the dissolution of freshly comminuted glacial
413 sediments preferentially release HCO_3^- and $(\text{Ca}^{2+}+\text{Mg}^{2+})$ (via hydrolysis of trace carbonates), it would
414 be expected that the HCO_3^- and $\text{Ca}^{2+}+\text{Mg}^{2+}$ ratios with respect to SO_4^{2-} would increase. The elevated
415 HCO_3^- could also result from the microbial oxidation of organic carbon (Wadham et al., 2010). The
416 higher intercepts of HCO_3^- v SO_4^{2-} , and $(\text{Ca}^{2+}+\text{Mg}^{2+})$ v SO_4^{2-} compared to LG, suggest rapid
417 acquisition of $(\text{Ca}^{2+}, \text{Mg}^{2+})$ and HCO_3^- in relation to SO_4^{2-} , potentially due to carbonate hydrolysis.
418 Also, during the Transition Period, the $(\text{Ca}^{2+}+\text{Mg}^{2+})$: HCO_3^- ratio increased to 1.50 (Fig. 7b), and the
419 SMF increased to ~0.18 (Supplementary Fig. 5). Collectively, these observations indicate some
420 influence from carbonate dissolution coupled to sulphide oxidation (Equation 5), similar to the Early
421 Season meltwaters at LG.

422 We see a prevalence of carbonate over silicate weathering during the Late Season at KS, providing
423 evidence of continuous availability of carbonate minerals within the subglacial system and a lack of
424 calcite saturation. Relationships close to 1:1 for $(\text{Ca}^{2+}+\text{Mg}^{2+})$: HCO_3^- (Fig. 7b) show that carbonation
425 of carbonates and carbonate hydrolysis are the dominate weathering reactions throughout the melt
426 season, as a 1:1 ratio is expected from Equation 2.

427 The values measured at KS are similar to bulk meltwaters of Alpine glaciers studied, although the
428 SO_4^{2-} concentrations in the outflow from KS are lower (Tranter et al., 2002). The overall major ion
429 relationships indicate a shift from carbonate hydrolysis (Equation 2) and coupled carbonate
430 dissolution-sulphide oxidation (Equation 5) to carbonation of carbonates as the melt season progresses,
431 with little evidence of enhanced silicate weathering.

432 **4.3 Catchment hydrology as a driver of $\delta^{30}\text{DSi}$ seasonal variability**

433 By combining our conceptual model of subglacial hydrology at LG and KS with the observed major
434 ion ratio chemistry, we can begin to understand the geochemical drivers behind variations in $\delta^{30}\text{Si}$
435 composition of the meltwaters in each catchment. An increased predominance of silicate dissolution
436 as the melt season progresses at LG should theoretically result in higher $\delta^{30}\text{DSi}$, as silicate weathering
437 and the formation of secondary weathering products preferentially incorporate the lighter isotopes into
438 the newly formed solid (De La Rocha et al., 2000; Frings et al., 2016). While this pattern is observed
439 in non-glacial regimes, the lowest $\delta^{30}\text{DSi}$ values measured at LG coincided with the most pronounced
440 silicate weathering signals, and likely, by association, the longest residence time waters. We
441 hypothesise that the low $\delta^{30}\text{DSi}$ values measured at LG after Day 170 reflect the dissolution of
442 isotopically light ASi and secondary weathering products in subglacially stored waters and/or the
443 dissolution of isotopically light fresh mineral surface layers formed by enhanced physical weathering
444 (Hawkings et al., 2018). As the melt season progressed, the hydrologically active part of the
445 catchment retreated further inland and more isolated subglacial waters became hydrologically
446 connected (Hawkings et al., 2015), resulting in decreasing $\delta^{30}\text{DSi}$ (Fig. 5b) and D:M ratios as
447 discharge rose (Fig. 5a). The declining D:M ratios indicate a move to increasingly dominant silicate
448 weathering and redissolution of secondary weathering products from the more isolated subglacial
449 system or longer residence time waters, resulting in more dissolution of these finely ground
450 weathering crusts, which results in the lowering of the $\delta^{30}\text{DSi}$ composition.

451 Some decline in $\delta^{30}\text{DSi}$ also occurred during the Transition Period at KS (Fig. 5c), which was likely
452 linked to the opening of subglacial hydrological pathways and flushing of a formerly distributed
453 drainage system. We would expect redissolution of secondary weathering products to occur at KS due
454 to the high pH and the undersaturation of ASi (Crompton et al., 2015, Supplementary Fig. 3).
455 However, $\delta^{30}\text{DSi}$ composition at KS is consistently higher than $\delta^{30}\text{ASi}$ and bedrock values (Fig. 4d),
456 indicating that the $\delta^{30}\text{DSi}$ exported is a result of fractionation due to net secondary weathering product
457 formation (Crompton et al., 2015). We hypothesise that the shorter residence times beneath KS
458 compared to LG reduce the potential for redissolution of secondary weathering products to occur. It
459 is more likely that there are fewer inland regions that remain isolated at KS, and the supraglacial
460 waters are routed more efficiently through the subglacial system.

461 KS and LG have broadly similar bedrock compositions (Hawkings et al., 2016), with any differences
462 unlikely to have a major impact on the overall $\delta^{30}\text{Si}$ composition of the measured bulk bedrock
463 (Savage et al., 2010). The intrusive rocks of the Julianhåb batholith and the Gardar Province at KS
464 would be expected to have a limited range in $\delta^{30}\text{Si}$ values due to minimal isotope fractionation during
465 high temperature mantle processes (Savage et al., 2010; Savage et al., 2014). Therefore, our
466 measurements of crushed proglacial rock debris for both catchments are in good agreement with the
467 published range of values measured in West Greenland (Andre et al., 2006). The measured mean
468 bedrock values of $\delta^{30}\text{Si}$ at KS are lighter compared to LG ($-0.18 \pm 0.06\%$ compared to $0.00 \pm 0.07\%$),

469 making them more comparable to values for bulk silicates on the Earth's surface ($-0.29 \pm 0.08\%$,
470 Savage et al. 2010). The heavier $\delta^{30}\text{Si}$ composition measured at LG could be an artefact of sampling
471 bedrock with a weathering crust, rather than pristine samples. However, basalts have a lower isotopic
472 composition (-0.3% to -0.2% , Georg et al., 2007; Chemtob et al., 2015), so it is possible KS bedrock
473 is isotopically lighter, as a result of basaltic intrusions. Nevertheless, we attribute variations in silicon
474 isotope composition of SPM ASi to be largely a result of weathering processes at the glacier bed. The
475 isotopic fractionations caused by weathering conditions has been shown to be much greater than any
476 variations in crustal samples, despite often significant differences in compositions (Ziegler et al., 2005;
477 Savage et al., 2010; Savage et al., 2013).

478 Neither catchment showed a seasonal trend in SPM $\delta^{30}\text{ASi}$, which exhibited a constant offset towards
479 lower values compared to our bulk bedrock measurements (~ 0.1 to 0.2% ; Fig. 5c, d). The offset could
480 be the result of fractionation induced precipitation reactions, weathering of silicate rocks,
481 comminution of particles, or a combination of all three (Andre et al., 2006; Chemtob et al., 2015). The
482 precipitation of ASi at low temperatures results in the preferential uptake of ^{28}Si into the solid phase
483 (e.g. Geiler et al. 2014). High resolution transmission electron microscope photomicrographs of ASi
484 in SPM show it to be associated with edges of particles and with elements such as Al and Fe,
485 suggesting it potentially forms as a result of aluminosilicate mineral weathering (Hellmann et al.,
486 2012; Hawkings et al., 2017). The presence of ASi with elevated Al/Si ratios indicates that it would
487 also be enriched in ^{28}Si , based on prior low temperature laboratory experiments (Oelze et al., 2015).
488 However, the offset in SPM $\delta^{30}\text{ASi}$ from the bedrock measurements could also be linked to physical
489 grinding, which has been demonstrated to result in the formation of reactive amorphous surface layers
490 (Lin and Somasundaran, 1972; Hawkings et al., 2017). ASi formed in this way is likely to be
491 characterised by isotopically light compositions as it is derived from the alteration of a freshly crushed
492 outer mineral layer, enriched in ^{28}Si , due to kinetic fractionation (Zielger et al., 2005). All three
493 processes result in ASi enriched in ^{28}Si , so our current data is unable to infer which of these is most
494 important as ASi from both catchments are lighter than bedrock values across the season.

495 **4.4 Understanding the Isotopic Mass Imbalance**

496 The interpretations presented above highlight a potential mass imbalance that arises because the
497 subglacial waters export both DSi and ASi that is isotopically lighter than bedrock values at LG. In
498 addition to this, when the $\delta^{30}\text{DSi}$ and $\delta^{30}\text{ASi}$ compositions at LG are summed, considering the relative
499 contributions of both, the total $\delta^{30}\text{Si}$ is consistently lighter than the measured bedrock across the melt
500 season. Whilst we have sampled the majority of the melt season at LG ($>60\%$), we did not continue
501 sampling until the shutdown of the subglacial system. Therefore, we have carried out a simple mass
502 balance calculation to ensure the mass imbalance seen at LG is not simply an artefact of the
503 unmonitored part of the season (Supplementary Table 5). Whilst we do not have geochemical data

504 past Day 210, we have a continuous discharge (Q) record until much later in the season. From this
505 record we calculated the proportion of the measured discharge compared to the total discharge. We
506 assumed that DSi concentrations were similar to the discharge weighted mean from the measured
507 period. As the $\delta^{30}\text{ASi}$ composition was relatively constant across the measured period, this trend
508 would likely continue into the latter stages of the season. We estimate the $\delta^{30}\text{Si}$ composition of the
509 unmeasured DSi required to ensure the total Si exported had a $\delta^{30}\text{Si}$ composition that matched the
510 bulk bedrock composition. The overall $\delta^{30}\text{Si}$ composition after the sampling period would need to be
511 +0.44‰, with a $\delta^{30}\text{DSi}$ composition of +2.22‰, in order to balance the $\delta^{30}\text{Si}$ composition over the
512 rest of the melt season. The aim of this simple calculation was to demonstrate whether the mass
513 imbalance could be realistically resolved by only considering the latter stages of the melt season,
514 which we were unable to sample. A $\delta^{30}\text{DSi}$ composition of +2.22‰ is likely unrealistic, considering
515 the range of values measured over the rest of the season are significantly lighter. It is therefore likely
516 the subglacial processes are driving the mass imbalance seen at LG.

517

518 One hypothesis to explain this mass imbalance is that the continuing light $\delta^{30}\text{DSi}$ values of bulk
519 meltwaters reflect physical erosion processes. High physical erosion of bedrock under the GrIS results
520 in the formation of fresh finely ground rock flour, with very high surface areas (Cowton et al., 2012;
521 Telling et al., 2015; Hawkings et al., 2016; Nienow et al., 2017). Published dissolution experiments
522 have shown there is a preferential dissolution of ^{28}Si from the fresh mineral surface, as a result of
523 kinetic fractionation (Ziegler et al., 2005). Therefore, we expect that the freshly crushed subglacial
524 minerals to result in delivery of dissolved silicon enriched in ^{28}Si . The high pH and under saturation of
525 waters with respect to ASi subsequently promotes the outer amorphous mineral layers to undergo
526 further dissolution, resulting in the export of light $\delta^{30}\text{DSi}$. The higher $\delta^{30}\text{DSi}$ composition at the
527 beginning of the season reflects the weathering environment at marginal areas of the ice sheet. These
528 areas are accessed more regularly by surface melt, with efficient hydrological drainage for longer
529 parts of the season (Chandler et al., 2013), and with potentially less active grinding of bedrock (as
530 demonstrated by lower suspended sediment concentrations during the Early Season). As the melt
531 season progresses, more isolated inland regions of the bed are accessed, where dissolution has
532 occurred over longer time periods and where physical erosion is enhanced, potentially evidenced by
533 the linear relationship between increasing SPM concentrations and decreasing $\delta^{30}\text{DSi}$ exported from
534 LG (Supplementary Fig. 6). Hence, the $\delta^{30}\text{DSi}$ of meltwaters exported is lower. By comparison, SPM
535 concentrations exported from KS are consistently lower. This could be a result of some settling in the
536 proglacial lake, but we believe it is more likely to result from lower rates of physical erosion in this
537 smaller catchment. We therefore hypothesise that higher physical erosion rates and longer residence
538 times in larger catchments (Wadham et al., 2010, Hawkings et al., 2016), help to explain the
539 differences in the $\delta^{30}\text{Si}$ composition of meltwaters from LG and KS.

540 To quantitatively assess if this hypothesis is realistic, we have modelled the proportion of DSi that
541 would need to result from the dissolution of ASi associated with SPM, assuming complete
542 dissolution, when considering the $\delta^{30}\text{Si}$ composition of the measured DSi and corresponding
543 endmembers (Equation 7). Our model was based on a range of fractionation factors for the initial
544 formation of ASi (ϵ) from the alteration of bedrock, as low temperature fractionation processes are
545 still poorly understood (Geilert et al., 2014; Frings et al., 2016). An open system was chosen, rather
546 than using Rayleigh fractionation, as we do not expect a finite pool of Si within the subglacial system
547 in the timescales we are considering.

548

549 The subglacial environment is complex; therefore, so we have simplified our model by assuming
550 overall fractionation during bedrock alteration to form ASi is similar to that observed during low
551 temperature ASi precipitation from solution with ϵ ranging from -2 ‰ to -5 ‰. Extrapolation from
552 experiments by Geilert et al. (2014) produces a fractionation factor of -2.34‰ at 0°C. However their
553 conclusions indicate that the fractionation factor at low temperatures is system dependent, due to
554 differences in fractionation based on external factors such as saturation state and surface area. Oelze
555 et al. (2015) found a fractionation factor of -5‰ for initial stages of experiments with high Al/Si
556 ratios, which could simulate subglacial conditions considering the potential formation of ASi through
557 aluminosilicate weathering (Hawkings et al., 2017). We use the first $\delta^{30}\text{DSi}$ value measured in the
558 Early Season at KS and a value measured at the subglacial portal in the Early Season at LG as the
559 initial $\delta^{30}\text{DSi}$ endmember in the model. The $\delta^{30}\text{ASi}$ endmember value is calculated by subtracting the
560 chosen fractionation factor from the $\delta^{30}\text{Si}$ composition of the bulk rock for each catchment.

561

562 In our modelled scenarios for LG we show that during outburst periods (and thus when $\delta^{30}\text{DSi}$
563 composition is lightest), a maximum of 56% of the measured DSi results from ASi dissolution (Fig. 8).
564 This proportion equates to $\sim 12\mu\text{M}$ of ASi compared to an overall ASi concentration of $\sim 290\mu\text{M}$
565 measured at the same timepoint, suggesting that even the maximum modelled values can be
566 considered reasonable due to the large ASi reservoir. Experimental data also suggest the most
567 negative ϵ values relate to solids formed rapidly and with unidirectional kinetic fractionation effects
568 (Oelze et al., 2015), which could also relate to these subglacial weathering crusts which are highly
569 reactive and would presumably undergo rapid dissolution. While all the modelled f_a values can be
570 considered realistic when converted to molar concentrations, we consider the lower values as more
571 representative of subglacial systems, considering the experimental data from Oelze et al. (2015).

572 Despite the lower ASi concentrations at KS, the modelled values can also be considered realistic for
573 this system. As we expect the ASi dissolution to be less important at KS compared to at LG, it follows
574 that we calculate lower proportions of ASi required to undergo dissolution in order to produce the
575 measured $\delta^{30}\text{DSi}$. We would expect the DSi at KS to be a result of silicate dissolution, from

576 hydrolysis reactions, with the formation of clay minerals as a secondary weathering product
577 (Crompton, 2015), as evidenced by increasing pH and the heavier $\delta^{30}\text{DSi}$ when compared to LG.

578 An alternative hypothesis to explain the mass imbalance at LG requires a temporal offset between
579 weathering product formation and re-dissolution. For example, the isotopically light secondary
580 weathering products may be a pre-glacial feature formed in a past, warmer climatic regime,
581 sequestered by an advancing ice sheet under a cooler climate and were stored subglacially (Hawkings
582 et al., 2018). The presence of palaeosols (>2.7million years, Bierman et al. 2014) beneath the ice
583 sheet, which are exported in runoff, supports the notion that there are pre-glacial features present
584 (Lawson et al., 2014; Kohler et al., 2017). The high pH of LG meltwaters (up to 9.63),
585 undersaturation of waters with respect to ASi, and high ASi concentrations (Qwt mean 209 μM after
586 Day 170), could result in the redissolution of these isotopically light amorphous secondary weathering
587 products when the isolated parts of the subglacial system become hydrologically connected
588 (Hawkings et al., 2018). Whilst this hypothesis provides explanation for the potential mass imbalance
589 and palaeosols are evidenced beneath ice sheets, it may be expected that this isotopically light source
590 of Si would get depleted over time and any enhanced weathering currently occurring *in-situ* would
591 result in heavier $\delta^{30}\text{DSi}$ exported in the meltwaters. Also, ASi measurements in the current proglacial
592 plain display very low concentrations (average 0.01wt%, Supplementary Table 6), suggesting these
593 amorphous phases are not currently being formed in the current proglacial environment, or have been
594 stripped away or aged. Therefore, whilst this hypothesis has potential to provide explanation for light
595 $\delta^{30}\text{DSi}$ compositions in glacial meltwaters, our data suggests our first hypothesis focusing on physical
596 erosion is currently the most likely scenario.

597 **4.5 Implications and Conclusions**

598 The two Greenland Ice Sheet (GrIS) catchments have different subglacial weathering regimes
599 primarily driven by subglacial hydrology. These weathering regimes appear related to water residence
600 time and therefore catchment size. Kiattuut Sermiat (KS) was dominated by carbonate hydrolysis,
601 whereas a predominance of silicate mineral weathering occurred as the melt season progressed at
602 Leverett Glacier (LG). Subglacial silicate weathering results in the production of isotopically light
603 amorphous secondary weathering solid phases in both catchments, with heavier isotopes recorded in
604 the dissolved fraction during Early Season meltwater discharge. As the melt season progressed, long
605 residence time subglacial waters became connected to an efficient drainage system. The larger of the
606 two catchments in this study, LG, exhibited a marked decrease in $\delta^{30}\text{DSi}$ from 0.87 to -0.55‰, as
607 meltwater discharge rose, and the subglacial drainage system expanded inland, tapping increasingly
608 remote subglacial water pockets. We interpret this isotopic shift as evidence of increasing contribution
609 from silicate weathering products, including the dissolution of ASi and other secondary weathering
610 products, and leaching of freshly crushed rock surfaces. The smaller catchment, KS, discharged

611 meltwaters with a $\delta^{30}\text{DSi}$ similar to smaller valley glaciers, with carbonate weathering the
612 predominant solute acquisition pathway.

613 Our results show that $\delta^{30}\text{DSi}$ and $\delta^{30}\text{ASi}$ can be used alongside major ion data to assess the degree of
614 silicate weathering, redissolution of weathering products and hydrological drainage characteristics in
615 glacial meltwaters. We postulate that access to meltwater present in subglacial drainage systems with
616 limited connection to an efficient drainage system will increase in the future, as snowlines retreat
617 further inland and melt increases under climatic warming (Hawkings et al., 2015). It is therefore likely
618 that the intensity of subglacial geochemical weathering and the composition of glacial waters entering
619 the ocean will be impacted. These findings are critical when attempting to estimate the fluxes of
620 nutrients from rapidly melting glaciated regions and their impact on elemental cycles, in the past (e.g.
621 during deglaciation events, Hawkings et al., 2018), present and future. The residence time of
622 subglacial waters will have an influence on the weathering reactions occurring, and therefore the
623 fluxes of key nutrients (Fe, P and Si) exported from glacial systems (Stevenson et al., 2017). More
624 robust estimation of Si fluxes and the $\delta^{30}\text{Si}$ composition of exported waters from the GrIS requires full
625 consideration and further study of catchment size, hydrological development, weathering regime, and
626 other processes within the complex subglacial system. The degree of silicate weathering in glaciated
627 regions may be much higher than previously thought, considering that it is the larger catchments that
628 discharge the majority of meltwater into the ocean from the GrIS and AIS. The quantity of meltwater
629 delivered Si from ice sheets and its isotopic composition should therefore be considered when
630 calculating global silicon budgets.

631 **Acknowledgements**

632 **This research is part of ERC funded project ICY-LAB (ERC-StG-ICY-LAB-678371), NERC**
633 **funded project DELVE (NERC grant NE/I008845/1) and a Leverhulme Trust Research Grant**
634 **(RPG-2016-439). JRH was additionally supported by the European Union's Horizon 2020**
635 **research and innovation programme under the Marie Skłodowska-Curie Actions fellowship**
636 **ICICLES (grant agreement #793962). Fieldwork was additionally supported by a Czech Science**
637 **Foundation Junior Grant (GACR 15-17346Y). TJK further supported by Charles University**
638 **Research Centre program No. 204069. Authors thank all those involved in fieldwork at Leverett**
639 **Camp and Kiattuut Sermiat Camps over both field seasons. We also thank the technical**
640 **support from Bristol Isotope Group (Dr. C. D. Coath, L. Cassarino and Dr. H. C. Ng) and**
641 **LOWTEX laboratories at the University of Bristol (J. Williams and Dr. F. Sgouridis). The**
642 **authors also thank the reviewers and associate editor for their comments to improve the**
643 **manuscript.**

644
645
646
647
648
649
650
651
652
653
654
655
656
657
658
659
660
661
662
663
664
665
666
667
668
669
670
671
672
673
674
675
676
677
678
679
680
681
682
683
684
685
686
687
688
689
690
691
692
693
694

References

- Andre L., Cardinal D., Alleman L. and Moorbath S. (2006) Silicon isotopes in ~3.8 Ga West Greenland rocks as clues to the Eoarchean supracrustal Si cycle. *Earth and Planetary Science Letters* **245**, 162-173.
- Bartholomew I., Nienow P., Sole A., Mair D., Cowton T., Palmer S. and Wadham J. (2011) Supraglacial forcing of subglacial drainage in the ablation zone of the Greenland ice sheet. *Geophysical Research Letters* **38**.
- Berner R.A. (2003) The long-term carbon cycle, fossil fuels and atmospheric composition. *Nature* **426**, 323.
- Bhatia M.P., Das S.B., Xu L., Charette M.A., Wadham J.L. and Kujawinski E.B. (2013) Organic carbon export from the Greenland ice sheet. *Geochim. Cosmochim. Acta* **109**, 329-344.
- Bierman P.R., Corbett L.B., Graly J.A., Neumann T.A., Lini A., Crosby B.T. and Rood D.H. (2014) Preservation of a Preglacial Landscape Under the Center of the Greenland Ice Sheet. *Science* **344**, 402-405.
- Bouysson P. (2014) Geological Map of the World at 1: 35 000 000, 3rd Edition ed. CCGM-CGMW.
- Cardinal D., Alleman L.Y., de Jong J., Ziegler K. and Andre L. (2003) Isotopic composition of silicon measured by multicollector plasma source mass spectrometry in dry plasma mode. *Journal of Analytical Atomic Spectrometry* **18**, 213-218.
- Cardinal D., Gaillardet J., Hughes H.J., Opfergelt S. and André L. (2010) Contrasting silicon isotope signatures in rivers from the Congo Basin and the specific behaviour of organic-rich waters. *Geophysical Research Letters* **37**.
- Chandler D.M., Wadham J.L., Lis G.P., Cowton T., Sole A., Bartholomew I., Telling J., Nienow P., Bagshaw E.B., Mair D., Vinen S. and Hubbard A. (2013) Evolution of the subglacial drainage system beneath the Greenland Ice Sheet revealed by tracers. *Nature Geosci* **6**, 195-198.
- Chemtob S.M., Rossman G.R., Young E.D., Ziegler K., Moynier F., Eiler J.M. and Hurowitz J.A. (2015) Silicon isotope systematics of acidic weathering of fresh basalts, Kilauea Volcano, Hawai'i. *Geochim. Cosmochim. Acta* **169**, 63-81.
- Conley D.J. (1998) An interlaboratory comparison for the measurement of biogenic silica in sediments. *Marine Chemistry* **63**, 39-48.
- Cowton T., Nienow P., Bartholomew I., Sole A. and Mair D. (2012) Rapid erosion beneath the Greenland ice sheet. *Geology* **40**, 343-346.
- Crompton J.W., Flower, G. E., Kirste, D., Hagedorn, B., and Sharp, M. J. (2015) Clay mineral precipitation and low silica in glacier meltwaters explored through reaction-path modelling. *Journal of Glaciology* **61**, 1061-1078.
- Das S.B., Joughin I., Behn M.D., Howat I.M., King M.A., Lizarralde D. and Bhatia M.P. (2008) Fracture Propagation to the Base of the Greenland Ice Sheet During Supraglacial Lake Drainage. *Science* **320**, 778-781.
- De La Rocha C.L., Brzezinski M., A. and DeNiro M.J. (2000) A first look at the distribution of the stable isotopes of silicon in natural waters. *Geochim. Cosmochim. Acta* **64**, 2467-2477.
- De la Rocha C.L., Brzezinski M.A. and DeNiro M.J. (1997) Fractionation of silicon isotopes by marine diatoms during biogenic silica formation. *Geochim. Cosmochim. Acta* **61**, 5051-5056.
- DeMaster D., J. (1981) The Supply and Accumulation of Silica in the Marine-Environment. *Geochim. Cosmochim. Acta* **45**, 1715-1732.
- Ding T., Wan D., Bai R., Zhang Z., Shen Y. and Meng R. (2005) Silicon isotope abundance ratios and atomic weights of NBS-28 and other reference materials. *Geochim. Cosmochim. Acta* **69**, 5487-5494.
- Ding T., Wan D., Wang C. and Zhang F. (2004) Silicon isotope compositions of dissolved silicon and suspended matter in the Yangtze River, China. *Geochim. Cosmochim. Acta* **68**, 205-216.
- Ding T.P., Gao J.F., Tian S.H., Wang H.B. and Li M. (2011) Silicon isotopic composition of dissolved silicon and suspended particulate matter in the Yellow River, China, with implications for the global silicon cycle. *Geochim. Cosmochim. Acta* **75**, 6672-6689.

695 Dubnick A., Kazemi S., Sharp M., Wadham J., Hawkings J., Beaton A. and Lanoil B. (2017) Hydrological
696 controls on glacially exported microbial assemblages. *Journal of Geophysical Research:*
697 *Biogeosciences* **122**, 1049-1061.

698 Escher A., Watt, W. S. (1976) Geology of Greenland, Grønlands Geologiske undersøgelse.

699 Fontorbe G., De La Rocha C.L., Chapman H.J. and Bickle M.J. (2013) The silicon isotopic composition
700 of the Ganges and its tributaries. *Earth and Planetary Science Letters* **381**, 21-30.

701 Frings P.J., Clymans W., Fontorbe G., De La Rocha C. and Conley D.J. (2016) The continental Si cycle
702 and its impact on the ocean Si isotope budget. *Chemical Geology* **425**, 12-36.

703 Gaillardet J., Dupré B., Louvat P. and Allègre C.J. (1999) Global silicate weathering and CO₂
704 consumption rates deduced from the chemistry of large rivers. *Chemical Geology* **159**, 3-30.

705 Geilert S., Vroon P.Z., Roerdink D.L., Van Cappellen P. and van Bergen M.J. (2014) Silicon isotope
706 fractionation during abiotic silica precipitation at low temperatures: Inferences from flow-through
707 experiments. *Geochim. Cosmochim. Acta* **142**, 95-114.

708 Georg R.B., Reynolds B.C., Frank M. and Halliday A.N. (2006) New sample preparation techniques for
709 the determination of Si isotopic compositions using MC-ICPMS. *Chemical Geology* **235**, 95-104.

710 Georg R.B., Reynolds B.C., West A.J., Burton K.W. and Halliday A.N. (2007) Silicon isotope variations
711 accompanying basalt weathering in Iceland. *Earth and Planetary Science Letters* **261**, 476-490.

712 Georg R.B., Zhu C., Reynolds B.C. and Halliday A.N. (2009) Stable silicon isotopes of groundwater,
713 feldspars, and clay coatings in the Navajo Sandstone aquifer, Black Mesa, Arizona, USA. *Geochim.*
714 *Cosmochim. Acta* **73**, 2229-2241.

715 Graly J., Harrington J. and Humphrey N. (2017) Combined diurnal variations of discharge and
716 hydrochemistry of the Isunnguata Sermia outlet, Greenland Ice Sheet. *The Cryosphere* **11**, 1131-1140.

717 Graly J.A., Humphrey N.F., Landowski C.M. and Harper J.T. (2014) Chemical weathering under the
718 Greenland Ice Sheet. *Geology* **42**, 551-554.

719 Harper J.T. and Humphrey N.F. (1995) Borehole video analysis of a temperate glacier' englacial and
720 subglacial structure: Implications for glacier flow models. *Geology* **23**, 901-904.

721 Hawkings J., Wadham J., Tranter M., Telling J., Bagshaw E., Beaton A., Simmons S.-L., Chandler D.,
722 Tedstone A. and Nienow P. (2016) The Greenland Ice Sheet as a hot spot of phosphorus weathering
723 and export in the Arctic. *Global Biogeochemical Cycles* **30**, 191-210.

724 Hawkings J.R., Hatton J.E., Hendry K.R., de Souza G.F., Wadham J.L., Ivanovic R., Kohler T.J., Stibal M.,
725 Beaton A., Lamarche-Gagnon G., Tedstone A., Hain M.P., Bagshaw E., Pike J. and Tranter M. (2018)
726 The silicon cycle impacted by past ice sheets. *Nature Communications* **9**, 3210.

727 Hawkings J.R., Wadham J.L., Benning L.G., Hendry K.R., Tranter M., Tedstone A., Nienow P. and
728 Raiswell R. (2017) Ice sheets as a missing source of silica to the polar oceans. *Nature*
729 *Communications* **8**, 14198.

730 Hawkings J.R., Wadham J.L., Tranter M., Lawson E., Sole A., Cowton T., Tedstone A.J., Bartholomew I.,
731 Nienow P., Chandler D. and Telling J. (2015) The effect of warming climate on nutrient and solute
732 export from the Greenland Ice Sheet. *Geochemical Perspectives Letters*, 94-104.

733 Hellmann R., Wirth R., Daval D., Barnes J.-P., Penisson J.-M., Tisserand D., Epicier T., Florin B. and
734 Hervig R.L. (2012) Unifying natural and laboratory chemical weathering with interfacial dissolution–
735 reprecipitation: A study based on the nanometer-scale chemistry of fluid–silicate interfaces.
736 *Chemical Geology* **294-295**, 203-216.

737 Hendry K. and Robinson L.F. (2012) The relationship between silicon isotope fractionation in sponges
738 and silicic acid concentration.: Modern and core-top studies of biogenic opal. *Geochim. Cosmochim.*
739 *Acta* **81**, 1-12.

740 Henriksen N., Higgins, A. K., Kalsbeek, F., and Pulvertaft, T. C. R. (2009) Greenland From Archaean to
741 Quaternary Descriptive Text to the 1995 Geological Map of Greenland, 1:2 500 000, Geol. Surv. Den.
742 Greenl., Geological Survey of Denmark and Greenland, 2nd Edition ed, Copenhagen, pp. 9-116.

743 Hindshaw R.S., Rickli J., Leuthold J., Wadham J. and Bourdon B. (2014) Identifying weathering
744 sources and processes in an outlet glacier of the Greenland Ice Sheet using Ca and Sr isotope ratios.
745 *Geochim. Cosmochim. Acta* **145**, 50-71.

746 Hoffman M.J., Catania G.A., Neumann T.A., Andrews L.C. and Rumrill J.A. (2011) Links between
747 acceleration, melting, and supraglacial lake drainage of the western Greenland Ice Sheet. *Journal of*
748 *Geophysical Research: Earth Surface* **116**.

749 Hughes H.J., Delvigne C., Korntheuer M., de Jong J., André L. and Cardinal D. (2011) Controlling the
750 mass bias introduced by anionic and organic matrices in silicon isotopic measurements by MC-ICP-
751 MS. *Journal of Analytical Atomic Spectrometry* **26**, 1892.

752 Kohler T.J., Zarsky J.D., Yde J.C., Lamarche-Gagnon G., Hawkings J.R., Tedstone A.J., Wadham J.L., Box
753 J.E., Beaton A.D. and Stibal M. (2017) Carbon dating reveals a seasonal progression in the source of
754 particulate organic carbon exported from the Greenland Ice Sheet. *Geophysical Research Letters* **44**,
755 6209-6217.

756 Lawson E.C., Wadham J.L., Tranter M., Stibal M., Lis G.P., Butler C.E.H., Laybourn-Parry J., Nienow P.,
757 Chandler D. and Dewsbury P. (2014) Greenland Ice Sheet exports labile organic carbon to the Arctic
758 oceans. *Biogeosciences* **11**, 4015-4028.

759 Lin I.J. and Somasundaran P. (1972) Alterations in properties of samples during their preparation by
760 grinding. *Powder Technology* **6**, 171-179.

761 Mair D., Willis I., Fischer U.H., Hubbard B., Nienow P. and Hubbard A. (2004) Hydrological controls on
762 patterns of surface, internal and basal motion during three "spring events": Haut Glacier d'Arolla,
763 Switzerland. *Journal of Glaciology* **49**, 555-567.

764 Michaud A.B., Skidmore M.L., Mitchell A.C., Vick-Majors T.J., Barbante C., Turetta C., vanGelder W.
765 and Priscu J.C. (2016) Solute sources and geochemical processes in Subglacial Lake Whillans, West
766 Antarctica. *Geology* **44**, 347-350.

767 Nienow P. (2014) The plumbing of Greenland's ice. *Nature* **514**, 38.

768 Nienow P., Sharp M. and Willis I.C. (1998) Seasonal changes in the morphology of the subglacial
769 drainage system, Haut Glacier d'Arolla, Switzerland. *Earth Surface Processes and Landforms* **23**, 825-
770 843.

771 Nienow P.W., Sole A.J., Slater D.A. and Cowton T.R. (2017) Recent Advances in Our Understanding of
772 the Role of Meltwater in the Greenland Ice Sheet System. *Current Climate Change Reports* **3**, 330-
773 344.

774 Oelze M., von Blanckenburg F., Bouchez J., Hoellen D. and Dietzel M. (2015) The effect of Al on Si
775 isotope fractionation investigated by silica precipitation experiments. *Chemical Geology* **397**, 94-105.

776 Opfergelt S., Burton K.W., Pogge von Strandmann P.A.E., Gislason S.R. and Halliday A.N. (2013)
777 Riverine silicon isotope variations in glaciated basaltic terrains: Implications for the Si delivery to the
778 ocean over glacial–interglacial intervals. *Earth and Planetary Science Letters* **369-370**, 211-219.

779 Reynolds B.C., Aggarwal J., André L., Baxter D., Beucher C., Brzezinski M.A., Engström E., Georg R.B.,
780 Land M., Leng M.J., Opfergelt S., Rodushkin I., Sloane H.J., van den Boorn S.H.J.M., Vroon P.Z. and
781 Cardinal D. (2007) An inter-laboratory comparison of Si isotope reference materials. *Journal of*
782 *Analytical Atomic Spectrometry* **22**, 561-568.

783 Sauer D., Saccone L., Conley D.J., Herrmann L. and Sommer M. (2006) Review of methodologies for
784 extracting plant-available and amorphous Si from soils and aquatic sediments. *Biogeochemistry* **80**,
785 89-108.

786 Savage P.S., Georg R.B., Armytage R.M.G., Williams H.M. and Halliday A.N. (2010) Silicon isotope
787 homogeneity in the mantle. *Earth and Planetary Science Letters* **295**, 139-146.

788 Savage P.S., Georg R.B., Williams H.M. and Halliday A.N. (2013) Silicon isotopes in granulite xenoliths:
789 Insights into isotopic fractionation during igneous processes and the composition of the deep
790 continental crust. *Earth and Planetary Science Letters* **365**, 221-231.

791 Stevenson E.I., Fantle M.S., Das S.B., Williams H.M. and Aciego S.M. (2017) The iron isotopic
792 composition of subglacial streams draining the Greenland ice sheet. *Geochim. Cosmochim. Acta* **213**,
793 237-254.

794 Telling J., Boyd E.S., Bone N., Jones E.L., Tranter M., MacFarlane J.W., Martin P.G., Wadham J.L.,
795 Lamarche-Gagnon G., Skidmore M.L., Hamilton T.L., Hill E., Jackson M. and Hodgson D.A. (2015) Rock
796 comminution as a source of hydrogen for subglacial ecosystems. *Nature Geoscience* **8**, 851.

797 Tranter M., Sharp M.J., Lamb H.R., Brown G.H., Hubbard B.P. and Willis I.C. (2002) Geochemical
798 weathering at the bed of Haut Glacier d'Arolla, Switzerland - A new model. *Hydrological Processes* **16**,
799 959-993.

800 Tranter M. and Wadham J.L. (2014) 7.5 - Geochemical Weathering in Glacial and Proglacial
801 Environments A2 - Holland, Heinrich D, in: Turekian, K.K. (Ed.), *Treatise on Geochemistry* (Second
802 Edition). Elsevier, Oxford, pp. 157-173.

803 Wadham J.L., Tranter M., Skidmore M., Hodson A.J., Priscu J., Lyons W.B., Sharp M., Wynn P. and
804 Jackson M. (2010) Biogeochemical weathering under ice: Size matters. *Global Biogeochemical Cycles*
805 **24**.

806 Walker J.C.G., Hays P.B. and Kasting J.F. (1981) A negative feedback mechanism for the long-term
807 stabilization of Earth's surface temperature. *Journal of Geophysical Research: Oceans* **86**, 9776-9782.

808 Yde J.C., Knudsen N.T., Hasholt B. and Mikkelsen A.B. (2014) Meltwater chemistry and solute export
809 from a Greenland Ice Sheet catchment, Watson River, West Greenland. *Journal of Hydrology* **519**,
810 2165-2179.

811 Ziegler K., Chadwick O.A., Brzezinski M.A. and Kelly E.F. (2005) Natural variations of $\delta^{30}\text{Si}$ ratios
812 during progressive basalt weathering, Hawaiian Islands. *Geochim. Cosmochim. Acta* **69**, 4597-4610.

813 Ziegler K., Chadwick O.A., Kelly E.F. and Brzezinski M.A. (2002) The $\delta^{30}\text{Si}$ values of soil weathering
814 profiles: Indicators of Si pathways at the lithosphere/hydro (bio) sphere interface. *Geochim.*
815 *Cosmochim. Acta* **66**, A881.

816
817 **Table 1: Hydrological comparison of two studied catchments.** Qwt = discharge weighted mean,
818 D:M = divalent to monovalent ion ratio, DSi = Dissolved silicate, ASi = Amorphous silica.
819

	Kiattuut Sermia (2013)	Leverett Glacier (2015)
Mean Q (m^3S^{-1})	22.80 ⁺	85.35
Total Q (km^3)	0.22 ⁺	1.45
Qwt Sus. Sediment (g L^{-1})	0.12 ⁺	0.87
Qwt pH	9.09	8.63
Qwt EC ($\mu\text{S cm}^{-1}$)	26.66 ⁺	12.25
Qwt D:M (μeq)	6.91	1.36
Qwt DSi (μM)	22.18	20.76
Qwt ASi (μM)	9.87	205.78
Qwt $\delta^{30}\text{DSi}$ (‰)	0.41	-0.25
Qwt $\delta^{30}\text{ASi}$ (‰)	-0.47	-0.22
Bulk Rock $\delta^{30}\text{Si}$ (‰)	-0.18	0.00 ⁺

820 ⁺Data previously published by Hawkings et al. (2016).

821

822 **Figure 1: Location of Kiattuut Sermiat and Leverett Glacier, from Hawkings et al. (2016).** Water
823 samples were collected at the locations marked in black from proglacial streams, as in Lawson et al.
824 (2014) and Hawkings et al. (2016). Hydrological monitoring was completed at points of stable
825 bedrock (white markers).

826 **Figure 2: Hydrological and Geochemical Time series for LG (black, A) and KS (red, B).** Vertical
827 black shading in A shows outburst events recorded during the melt season (Kohler et al., 2017) and
828 vertical red shading in B shows the “Spring Event” at KS (Hawkings et al., 2016).

829 **Figure 3: Major ion ratio time series.** Ratio of Divalent/Monovalent ions (D:M) Differences in the
830 seasons (i.e. Late and Early Season) are defined by differences in hydrological and geochemical data
831 in the proglacial river.

832 **Figure 4: Na-normalised molar ratio mixing diagrams.** Silicate and carbonate endmembers taken
833 from Gaillardet et al. (1999) and references within, using data from small rivers draining one single
834 lithology.

835 **Figure 5: Silicon isotope composition results.** A) The relationship between $\delta^{30}\text{DSi}$ and D:M ion
836 ratio. B) $\delta^{30}\text{DSi}$ and discharge for both catchments. C and D) Time series of $\delta^{30}\text{DSi}$ and $\delta^{30}\text{ASi}$ for KS
837 and LG. Vertical blue shading in C indicates opening of the subglacial drainage system (“Spring
838 Event”, Hawkings et al. (2016)) and outburst events in D. Bulk bedrock $\delta^{30}\text{Si}$ is indicated by the
839 horizontal dashed line, with the shading representing 2SD. All error bars represent 2SD of external
840 errors (0.08 for $\delta^{30}\text{DSi}$ and 0.14 for $\delta^{30}\text{ASi}$).

841 **Figure 6: Diagram to illustrate conceptual model of subglacial hydrology development.**
842 Simplified development of subglacial hydrology at LG as the melt season progresses. Panel A
843 represents processes during the Early season of LG (before the first outburst event), B represents the
844 system after the first outburst event and subglacial water influences the proglacial stream chemistry,
845 and C represents the system during the late season once the snowline has retreated further and
846 outburst events occur more often. The smaller size of KS limits the subglacial hydrology development
847 to A and B, without the connection of isolated subglacial water by supraglacial lake drainage.

848 **Figure 7: Major ion relationship plots.** A) $\text{Ca}^{2+} + \text{Mg}^{2+}$ versus SO_4^{2-} B) $\text{Ca}^{2+} + \text{Mg}^{2+}$ versus HCO_3^- C)
849 HCO_3^- versus SO_4^{2-} . Early Season at KS is defined as before the subglacial system connected (Day
850 157, Hawkings et al. (2016)), Transition Period is the hydrologically unique period after the
851 subglacial connection and Late Season is post Day 169. Early season at LG is defined at prior to first
852 outburst event/subglacial connectivity at day 170 and late season is defined as day 170 onwards. Grey
853 dashed lines show main relationships found by Tranter et al. (2002) when studying an Alpine valley
854 glacier. The table outlines the regression slopes, intercepts and R^2 values for each relationship.

855 **Figure 8: Modelled Percentage ASi required for measured $\delta^{30}\text{DSi}$ composition.** Panels A and B
856 show the calculated f_a values according to Equation 7, with A (black) showing the time series at LG
857 and B (red) showing the time series at KS. ϵ values represent the varying fractionation factors used in
858 the model. Panels C (LG) and D (KS) show the concentration of ASi required to produce the
859 measured DSi, compared to the measured ASi concentrations over the melt season.

860 **Supplementary Figure 1: Estimated lake Residence Time at KS.** Residence time of the proglacial
861 lake at KS estimated by calculating the turnover rate of the lake using the estimated water volume of
862 the lake and river discharge.

863 **Supplementary Figure 2: Silicon three Isotope plot.** All samples analysed during the study are
864 included with red dashed lines showing the 95% prediction band and grey lines showing the 95%
865 confidence band. The black regression line has a gradient of 0.5118 ($p < 0.0001$, $R^2 = 0.9946$), showing
866 mass dependent fractionation

867 **Supplementary Figure 3: Relationship between $\delta^{30}\text{DSi}$ composition and saturation index of
868 amorphous silica.** Saturation indices calculated using Geochemists Workbench Software and plotted
869 against $\delta^{30}\text{DSi}$ for both catchments. Data has been split into the defined hydrological periods of the
870 melt season to show the temporal trend.

871 **Supplementary Figure 4: Comparison of geochemical data with previously published data at
872 LG.** Records of discharge, D:M ratio and SO_4^{2-} from LG in 2009 (Hindshaw et al., 2014) and 2015
873 (this study).

874 **Supplementary Figure 5: Sulphate Mass Fraction Timeseries.** Calculated SMF for KS and LG
875 over the melt season, with the seasons defined by hydrogeochemical data.

876 **Supplementary Figure 6: Relationship between SPM concentrations and dissolved silicon**
877 **isotope composition.**

Supplementary Tables

- 1 **Supplementary Table 1: Selected ionic concentrations from Leverett Glacier 2015, corresponding to timepoints in which silicon isotope measurements**
- 2 **were made.**

Decimal Day	Na⁺ (μeq)	K⁺ (μeq)	Mg²⁺ (μeq)	Ca²⁺ (μeq)	Al³⁺ (μeq)	SO₄²⁻ (μeq)	NO₃⁻ (μeq)	HCO₃⁻ (μeq)	F⁻ (μeq)	Cl⁻ (μeq)
128.4	53.84	36.79	98.64	349.25	-	229.58	0.35	271.80	2.11	30.98
135.4	41.04	26.68	61.27	215.01	1.66	118.64	0.39	200.01	0.93	20.05
140.8	56.16	38.59	41.59	126.20	4.06	75.20	0.44	256.49	1.22	37.1
145.4	64.46	39.38	73.43	252.03	-	117.65	0.35	286.19	1.53	19.94
148.4	46.21	30.20	52.09	183.94	5.59	88.86	0.33	203.98	1.08	1487
153.4	88.11	48.69	52.26	262.81	2.03	161.33	0.15	260.72	3.14	24.90
160.4	67.06	38.06	42.93	220.05	12.62	122.06	0.31	222.43	1.90	18.24
165.4	49.13	25.40	24.07	123.15	2.50	59.27	0.08	145.82	1.18	14.58
171.4	55.46	28.05	20.89	102.54	1.56	47.75	0.18	143.14	1.07	12.95
174.7	44.83	16.96	13.71	58.35	1.98	24.71	0.16	87.43	1.31	18.68
178.4	65.73	29.85	19.74	87.76	20.78	45.21	0.08	148.22	1.43	7.25
183.4	66.15	37.57	20.31	83.19	22.94	37.66	0.16	159.93	1.54	6.24
186.4	50.78	24.61	14.56	65.33	-	26.79	0.19	119.10	0.92	6.34
189.4	47.50	20.29	13.47	60.33	139.81	23.70	0.15	111.80	0.94	3.48
191.4	48.82	22.10	15.99	75.44	15.09	31.13	0.18	124.23	0.98	4.05
196.3	36.56	16.10	13.40	65.53	16.01	25.13	0.13	99.53	0.85	4.59
200.4	44.98	20.55	12.40	73.24	61.02	38.46	0.09	105.85	0.98	4.83
207.4	52.17	23.93	13.88	89.36	58.96	45.75	0.10	128.46	1.46	2.53
208.4	59.20	26.68	14.14	106.63	69.25	54.22	0.10	146.83	1.35	3.09
210.3	53.30	24.34	16.37	95.11	78.68	47.20	0.12	136.60	1.38	2.64

- 3
- 4
- 5
- 6

7 **Supplementary Table 2: Selected ionic concentrations from Kiattuut Sermiat 2013, corresponding to timepoints in which silicon isotope measurements**
 8 **were made.**

Decimal Day	Na ⁺ (μeq)	K ⁺ (μeq)	Mg ²⁺ (μeq)	Ca ²⁺ (μeq)	Al ³⁺ (μeq)	SO ₄ ²⁻ (μeq)	NO ₃ ⁻ (μeq)	HCO ₃ ⁻ (μeq)	F ⁻ (μeq)	Cl ⁻ (μeq)
111.59	47.92	29.14	63.53	442.50	5.10	66.13	0.07	477.37	19.01	24.51
124.48	45.32	28.32	53.57	404.70	-	70.94	0.23	417.08	18.15	22.96
139.50	45.22	29.46	54.62	378.04	-	75.97	0.23	387.05	17.65	23.91
149.50	46.24	29.47	56.42	397.38	-	82.29	0.32	398.28	18.39	26.13
150.50	42.33	27.46	51.81	373.51	6.64	82.68	0.32	363.79	19.03	25.91
155.52	42.37	27.34	49.55	358.36	7.24	73.93	0.30	359.86	16.12	24.21
159.50	36.44	24.16	42.55	296.01	-	59.01	0.26	303.08	12.14	21.92
162.63	30.68	21.43	36.56	264.80	-	50.45	0.26	268.78	11.86	19.41
170.90	24.47	18.84	28.39	224.87	17.44	29.96	0.19	251.22	9.11	12.73
172.68	22.96	18.03	27.04	224.71	19.92	26.37	0.16	244.61	8.57	11.29
178.50	21.14	17.23	26.89	227.25	-	22.92	0.15	250.96	7.44	9.39
181.50	19.95	16.37	25.15	226.12	-	22.27	0.12	246.50	8.09	9.24
194.52	18.88	14.46	25.91	218.87	-	20.43	0.09	240.61	8.43	7.47
205.54	15.01	11.96	21.04	179.89	-	14.43	0.08	200.92	6.53	4.99
207.50	13.18	10.44	17.51	147.3	-	13.76	0.09	161.89	6.71	4.99
212.53	14.65	11.22	19.34	181.91	13.53	15.05	0.06	198.67	7.41	5.26
220.63	13.56	10.52	17.92	167.17	11.73	15.04	0.05	180.46	7.82	5.17
221.6	13.14	11.01	16.93	164.53	-	14.15	0.03	191.17	6.68	4.57

9

10

11

12 **Supplementary Table 3: Summary of Kiattuut Sermiat silicon isotope results from 2013.**

Decimal Day	Discharge (m ³ s ⁻³)	pH	Suspended Sediment (g L ⁻¹)	DSi (μM)	δ ³⁰ DSi (‰)	δ ³⁰ DSi error * (2σSD ‰)	ASi (wt%)	δ ³⁰ ASi (‰)	δ ³⁰ ASi error * (2σSD ‰)	Monovalent/ Divalent ions (μeq L ⁻¹)
111.6	0.7	8.29	0.04	40.59	1.01	0.05				6.57
124.5	2.6	7.79	0.04	39.29	0.79	0.18				6.22
139.5	3.6	8.08	0.11	36.60	0.71	0.08				5.79
149.5	7.0	7.94	0.25	38.45			0.24	-0.56	0.05	5.99
150.5	7.1	8.02	0.15	36.14	0.69	0.11				6.09
155.5	17.9	8.23	0.16	34.62	0.64	0.09				5.85
159.5	34.5	8.86	0.18	28.33			0.37	-0.54	0.05	5.59
162.6	27.6	8.85	0.13	26.76	0.47	0.10				5.78
170.9	34.4	9.19	0.13	22.70			0.05	-0.38	0.07	6.05
172.7	33.3	9.25	0.11	21.84	0.26	0.11				6.14
178.5	18.5	9.38	0.13	20.69			0.36	-0.42	0.06	6.62
181.5	19.5	9.38	0.12	20.90	0.25	0.11				6.92
194.5	43.3	9.46	0.10	20.68	0.38	0.08	0.16	-0.48	0.06	7.34
205.5	42.9	9.08	0.09	16.49	0.57	0.02				7.45
207.5	37.7	9.08	0.10	16.00			0.26	-0.42	0.06	6.98
212.5	36.2	9.13	0.10	16.49	0.41	0.09	0.24			7.78
220.6	29.9	9.48	0.08	16.79	0.16	0.14				7.67
221.6	29.9	9.34	0.09	15.92			0.18	-0.56	0.05	7.67

13 *Propagated internal error (2σ SD, ‰)

14

15

16

17

18 **Supplementary Table 4: Summary of Leverett Glacier silicon isotope results from 2015.**

19

Decimal Day	Discharge (m ³ s ⁻³)	pH	Suspended Sediment (g L ⁻¹)	DSi (μM)	δ ³⁰ DSi (‰)	δ ³⁰ DSi error * (2σSD ‰)	ASi (wt%)	δ ³⁰ ASi (‰)	δ ³⁰ ASi error * (2σSD ‰)	Monovalent/Divalent ions (μeq L ⁻¹)
128.4	-	8.98	-	53.66	0.85	0.04	-	-	-	4.94
135.4	-	7.88	-	36.01	0.87	0.04	0.85	0.05	0.05	4.08
140.8	-	8.35	-	38.86	-		1.41	0.21	0.03	3.42
145.4	-	7.90	-	38.47	0.65	0.03	1.40	-0.16	0.03	3.13
148.4	5.4	7.72		35.63	-	-	-	-	-	3.09
153.4	13.0	7.85	0.54	37.00	0.66	0.04	1.03	-	-	2.30
160.4	17.5	7.80	0.53	31.51	0.60	0.02	0.75	-	-	2.34
165.4	25.1	7.64	0.56	24.13	0.37	0.03	0.86	-0.19	0.03	1.98
171.4	73.2	8.01	1.18	20.24	0.02	0.08	0.64	-	-	1.48
174.7	90.0	7.63	0.72	15.05	-0.23	0.02	-	-	-	1.17
178.4	122.7	8.41	1.37	24.85	-0.18	0.03	0.69	-0.20	0.04	1.12
183.4	215.1	9.18	2.09	27.69	-0.52	0.02	0.39	-0.15	0.03	1.00
186.4	207.2	8.33	0.85	19.75	-0.41	0.03	0.70	-	-	1.14
189.4	294.5	8.76	0.97	17.79	-0.41	0.03	0.83	-	-	1.09
191.4	360.9	9.24	1.05	21.41	-0.22	0.03	0.59	-0.27	0.04	1.29
196.3	230.1	8.58	0.66	16.29	-0.55	0.04	0.64	-	-	1.50
200.4	311.3	8.86	0.66	19.70	-0.14	0.03	0.85	-0.32	0.03	1.31
207.4	301.9	9.53	0.70	22.02	-	-	0.54	-0.16	0.04	1.36
208.4	270.5	9.62	0.78	24.83	-0.09	0.03	0.31	-	-	1.41
210.3	236.3	9.51	0.83	23.63	-0.06	0.03	0.97	-0.11	0.03	1.44

20 *Propagated internal error (2σ SD, ‰)

21

22

23 **Supplementary Table 5: Summary of Measured and Calculated values for Mass Balance Calculations at LG.**

	Up to Day 210	After Day 210*	Total*	24
Q (L)	1.27×10^{12}	6.04×10^{11}	1.88×10^{12}	25
% of Q for melt period	67.8	32.2	100	26
DSi Flux (μMol)	2.65×10^{13}	1.26×10^{13}	3.90×10^{13}	27
ASi Flux (μMol)	2.65×10^{14}	1.25×10^{14}	3.90×10^{14}	28
Total Si Flux (μMol)	2.91×10^{14}	1.38×10^{14}	4.29×10^{14}	29
% of DSi Flux for melt period	9.1	9.1	9.1	30
% of ASi Flux for melt period	90.9	90.9	90.9	31
				32
Qwt $\delta^{30}\text{DSi}$ (‰)	-0.25	+2.20	NA	33
Qwt $\delta^{30}\text{ASi}$ (‰)	-0.22	-0.22	NA	34
Total $\delta^{30}\text{Si}$ (‰)	-0.21	+0.44	0.00	

35 * All calculated values, except for Q, based on the percentage of Q measured before and after Day 210.

36

37 **Supplementary Table 6: Details of ASi concentrations taken from selected proglacial debris in front of LG.**

Sample Number	Date of Collection	Location	ASi (%)
1	30/5/2015	N67 03.909 W050 09. 795	0.02
2	30/5/2015	N67 03.912 W050 09.789	>0.01
6	2/6/2105	N67 03.758 W050 12.093	0.01

38

Figure 1

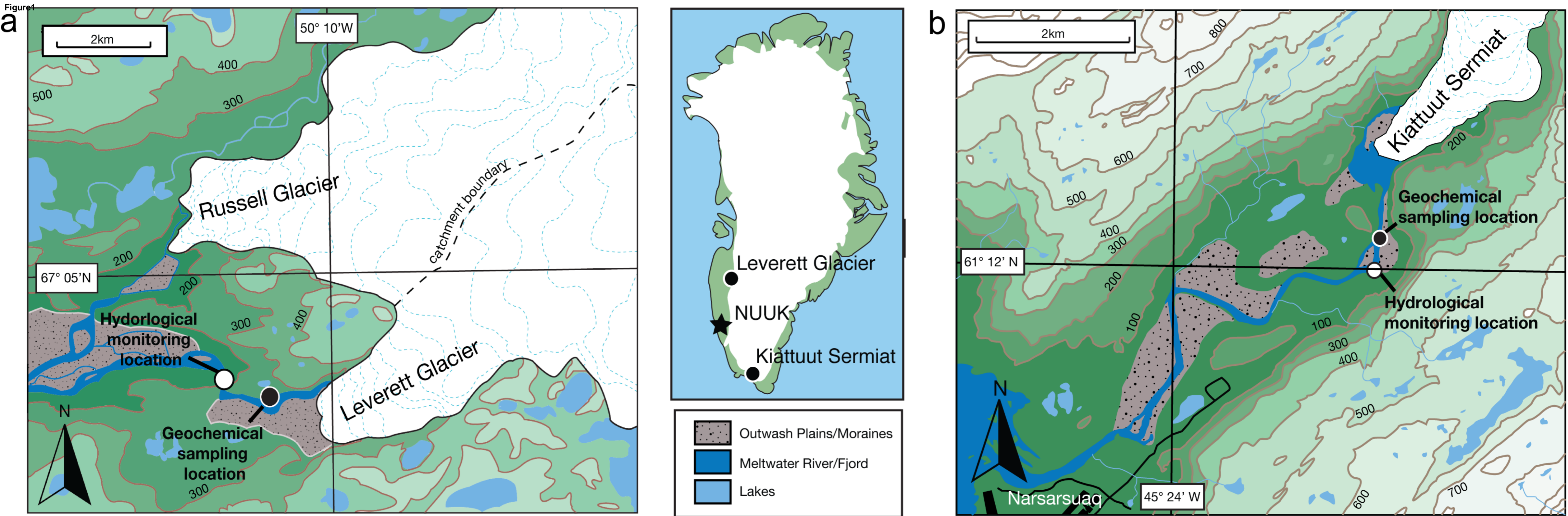


Figure2

[Click here to download high resolution image](#)

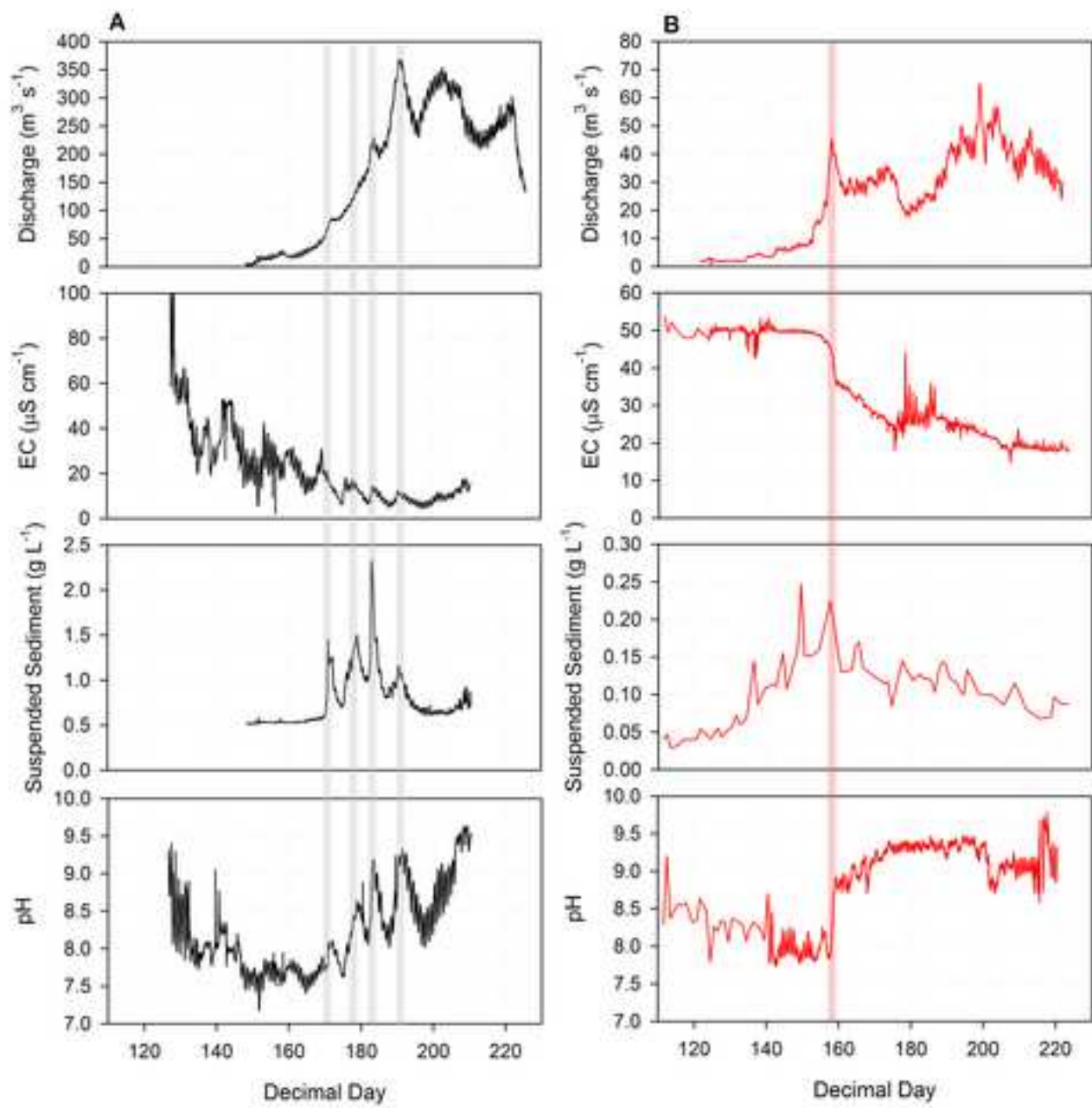


Figure3

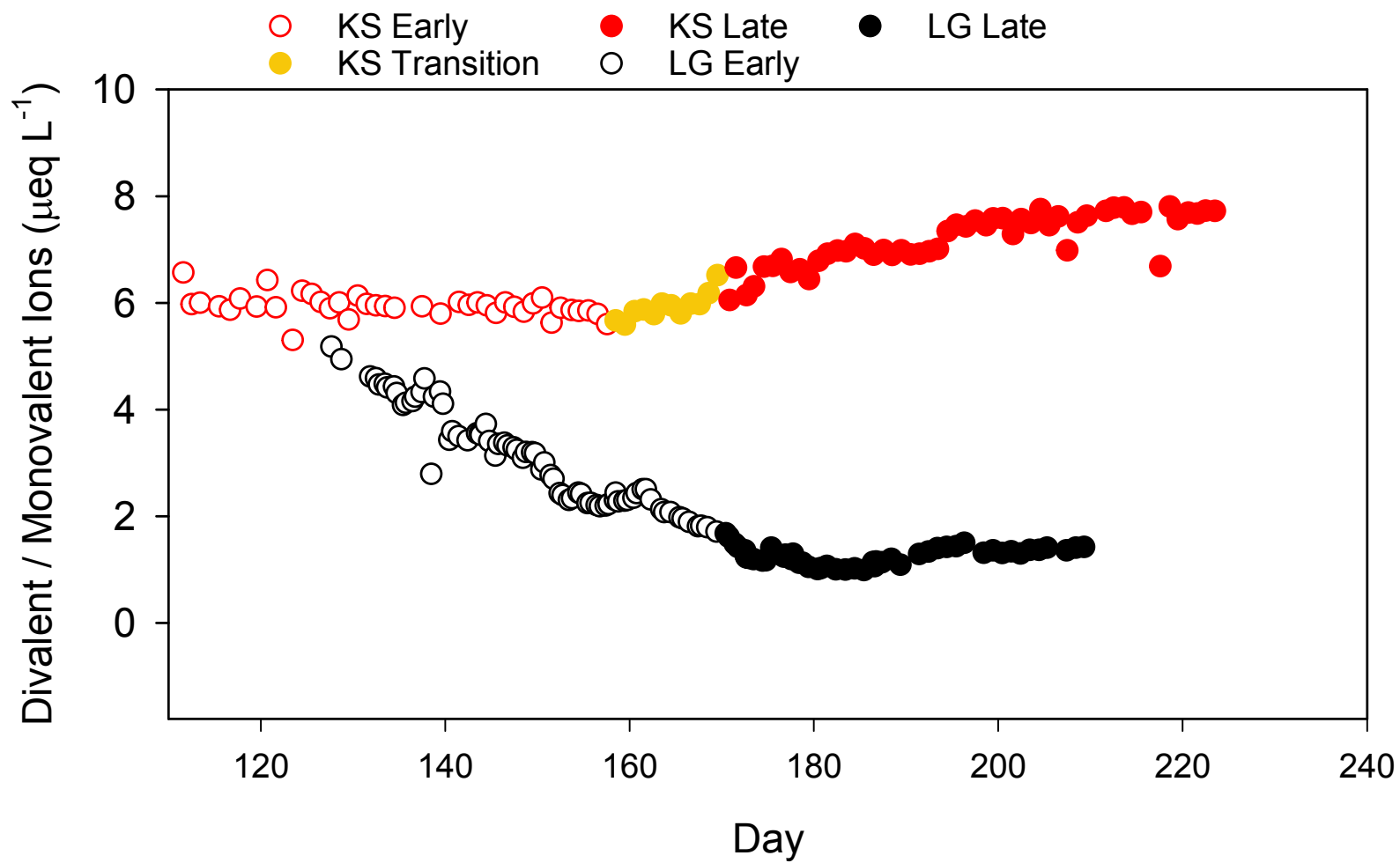


Figure 4

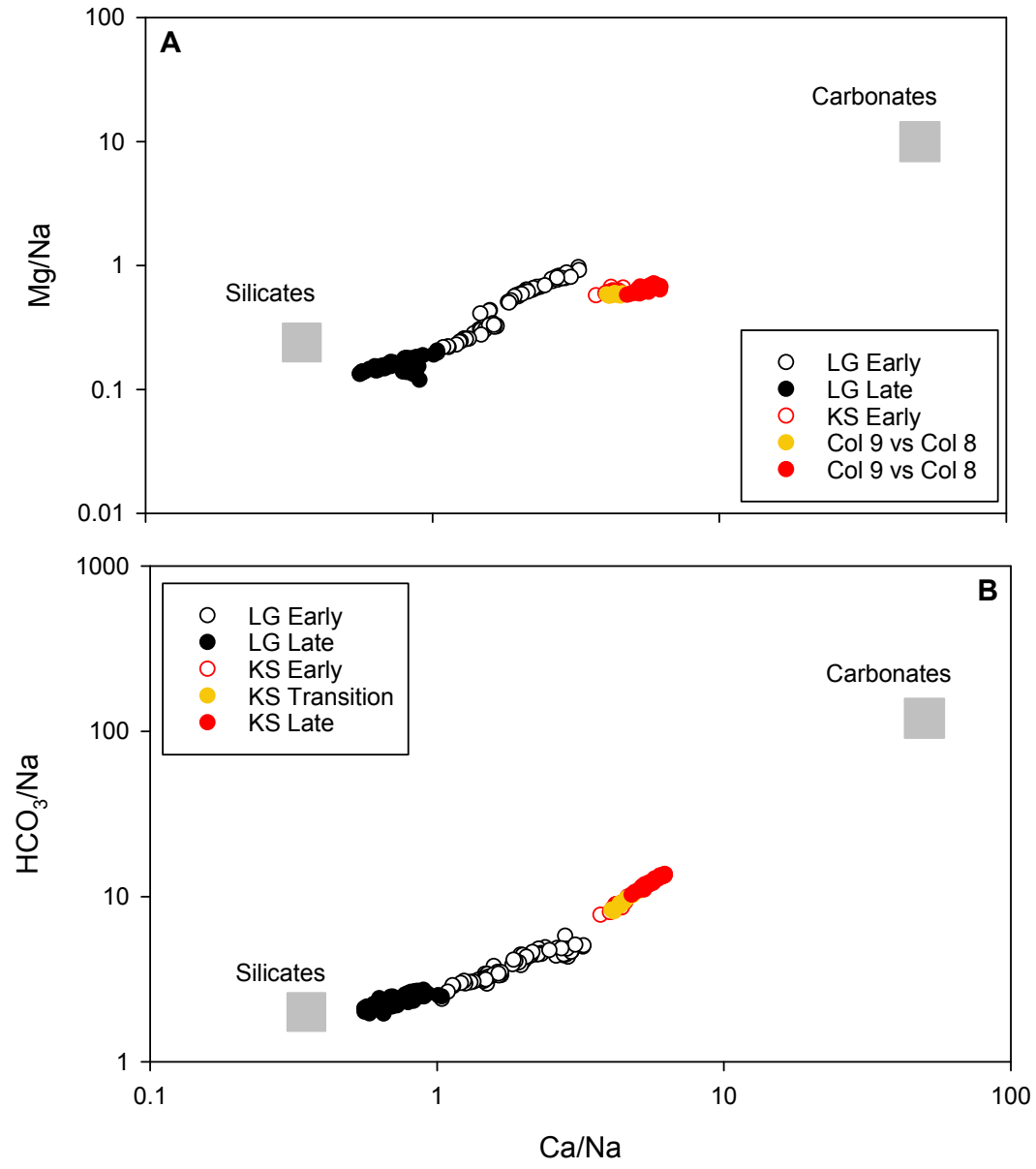


Figure5
[Click here to download high resolution image](#)

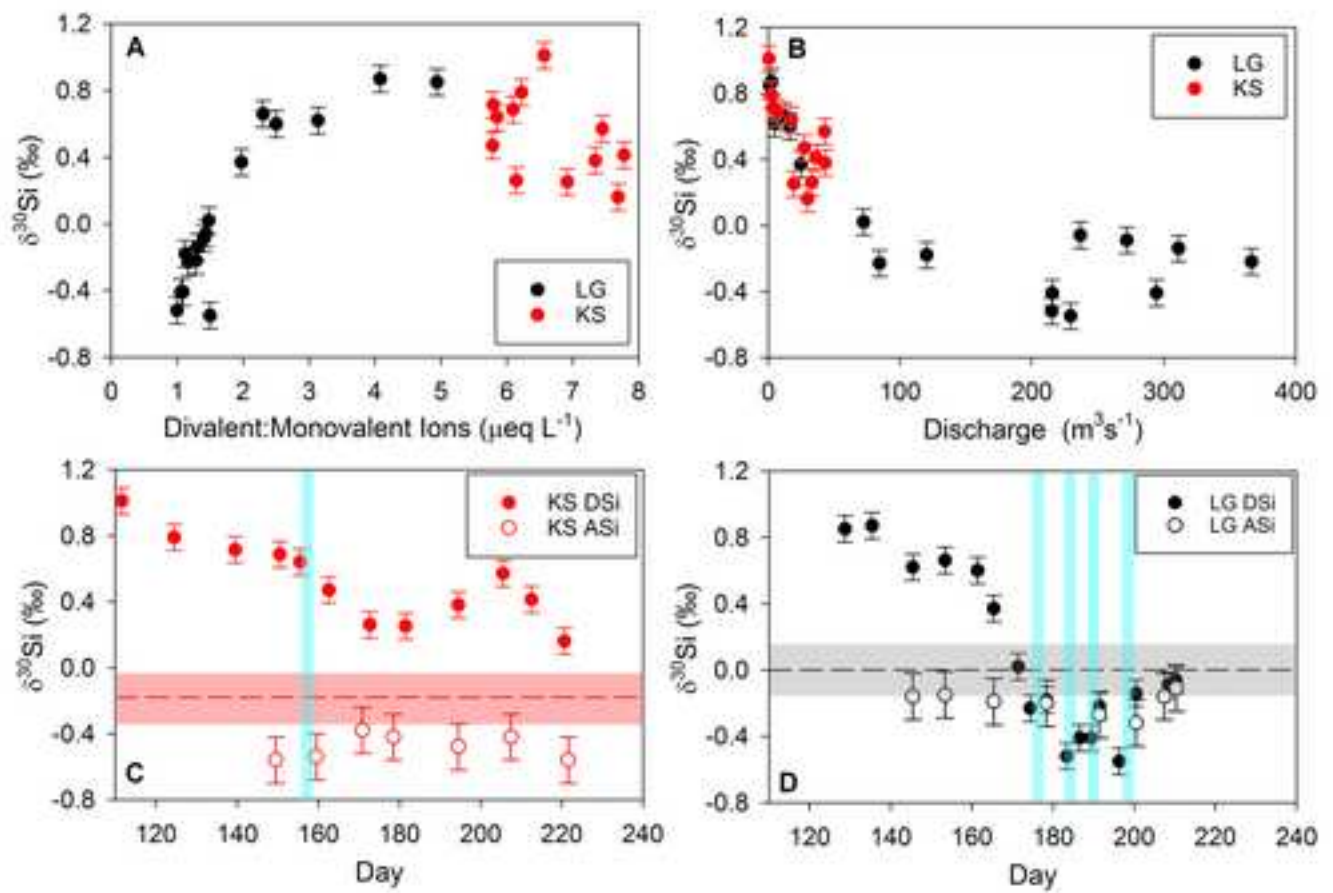


Figure 6

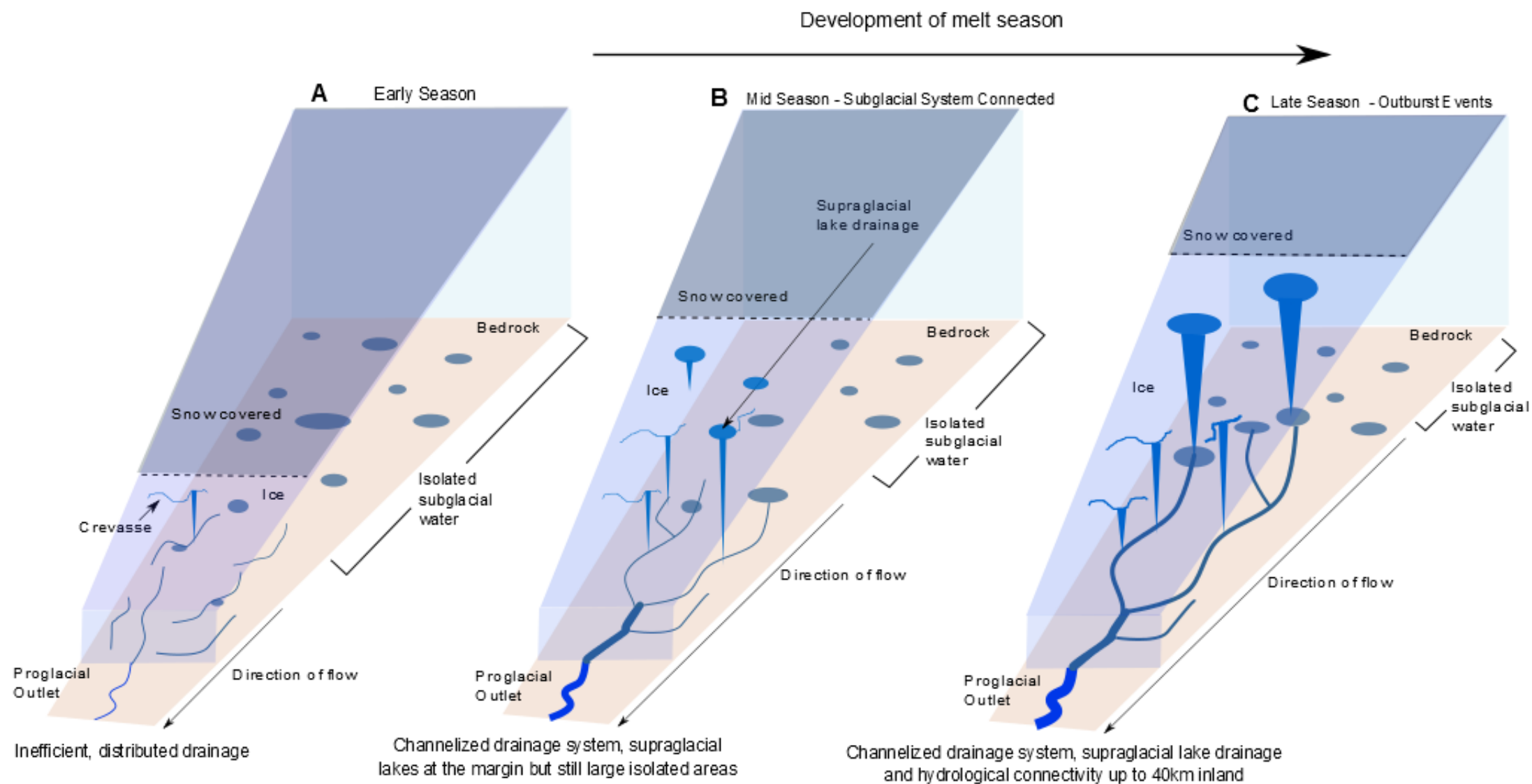
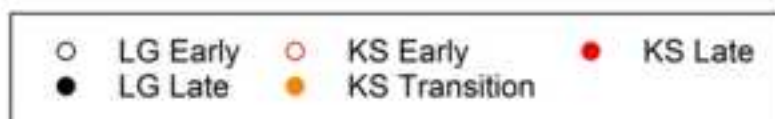
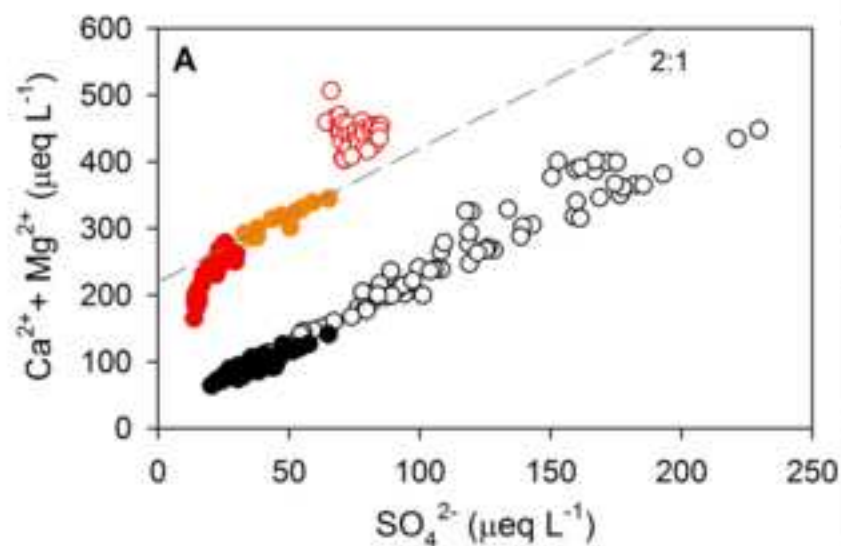


Figure 7

[Click here to download high resolution image](#)



		$\text{HCO}_3^- / \text{SO}_4^{2-}$	$(\text{Ca}^{2+} + \text{Mg}^{2+}) / \text{SO}_4^{2-}$	$(\text{Ca}^{2+} + \text{Mg}^{2+}) / \text{HCO}_3^-$
KS Early	Gradient	-1.58	-0.32	0.81
	Intercept	514	465	120
	R ² Value	0.1359	0.0076	0.9109
KS Transition	Gradient	0.82	1.82	1.50
	Intercept	247	227	-115
	R ² Value	0.4735	0.8585	0.8224
KS Late	Gradient	5.53	0.04	1.05
	Intercept	114	109	-5.69
	R ² Value	0.7634	0.8259	0.9927
LG Early	Gradient	0.95	1.92	1.52
	Intercept	95.4	38.1	-52.3
	R ² Value	0.6461	0.9354	0.8231
LG Late	Gradient	1.17	1.52	0.83
	Intercept	80.2	38.8	-7.57
	R ² Value	0.4941	0.8586	0.768

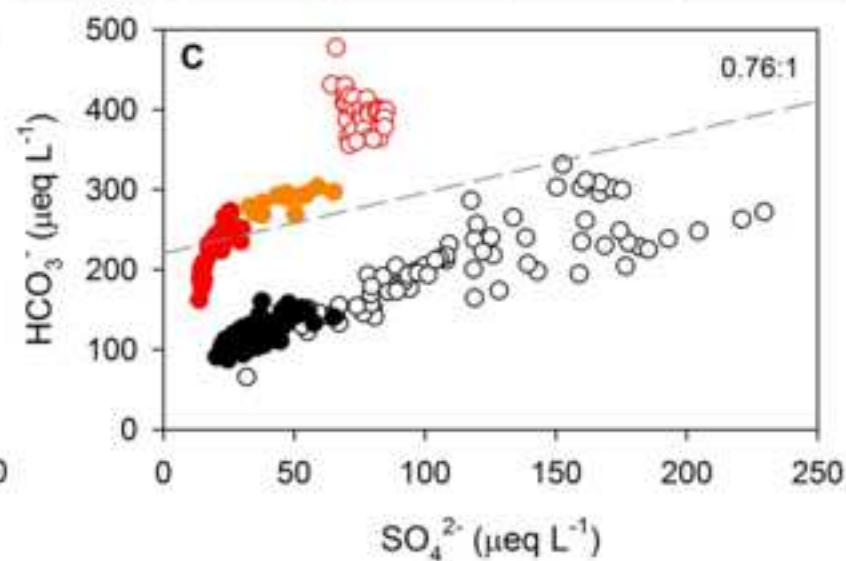
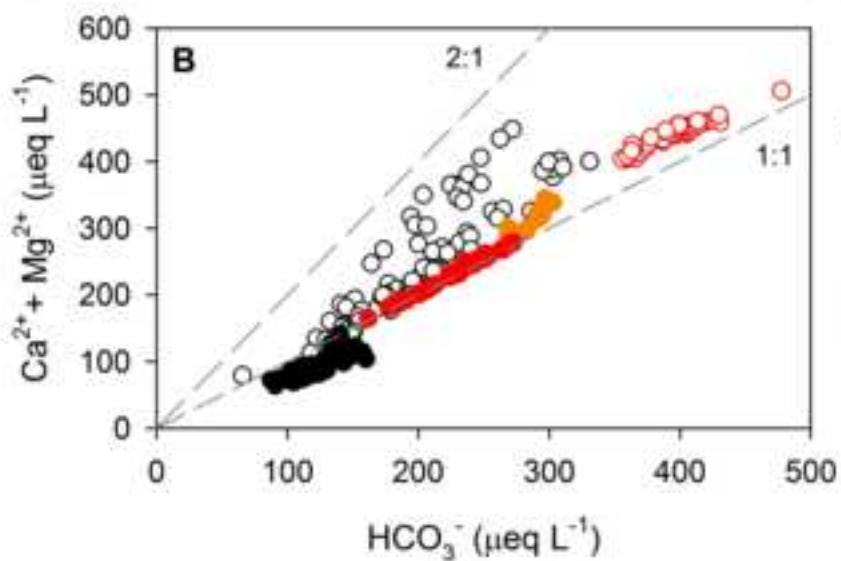
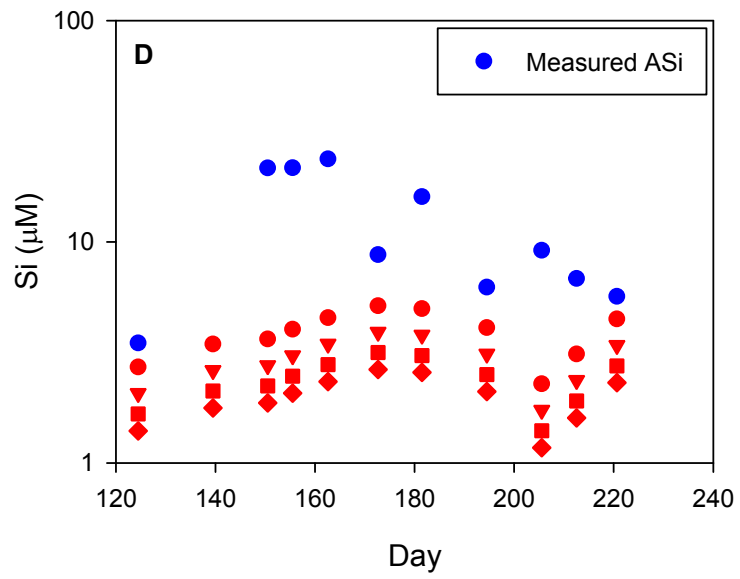
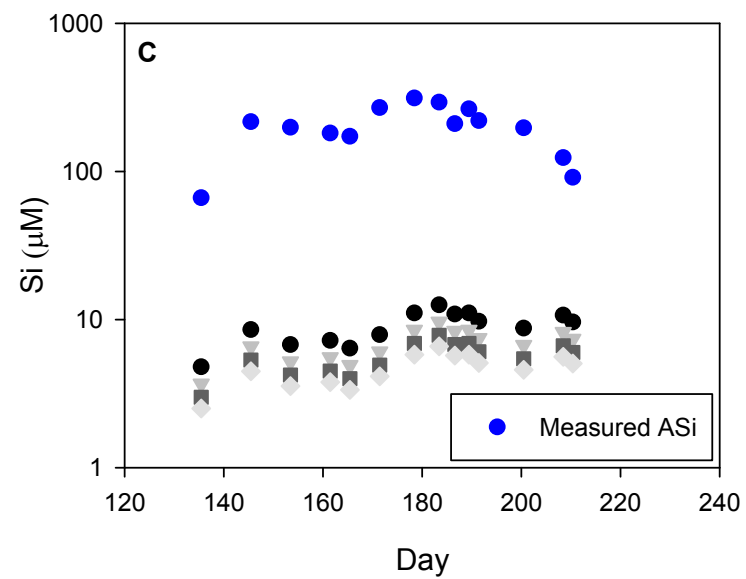
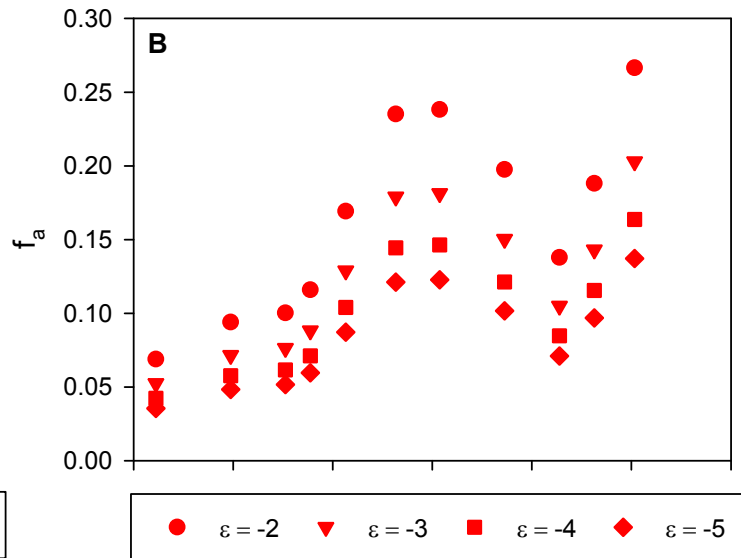
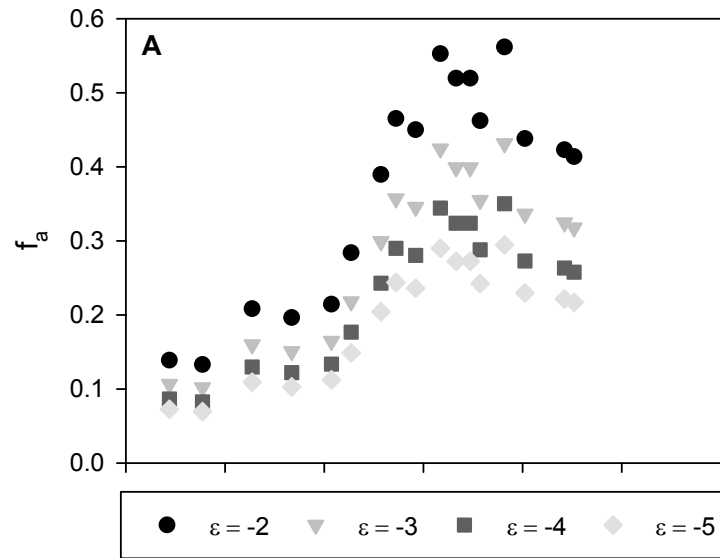
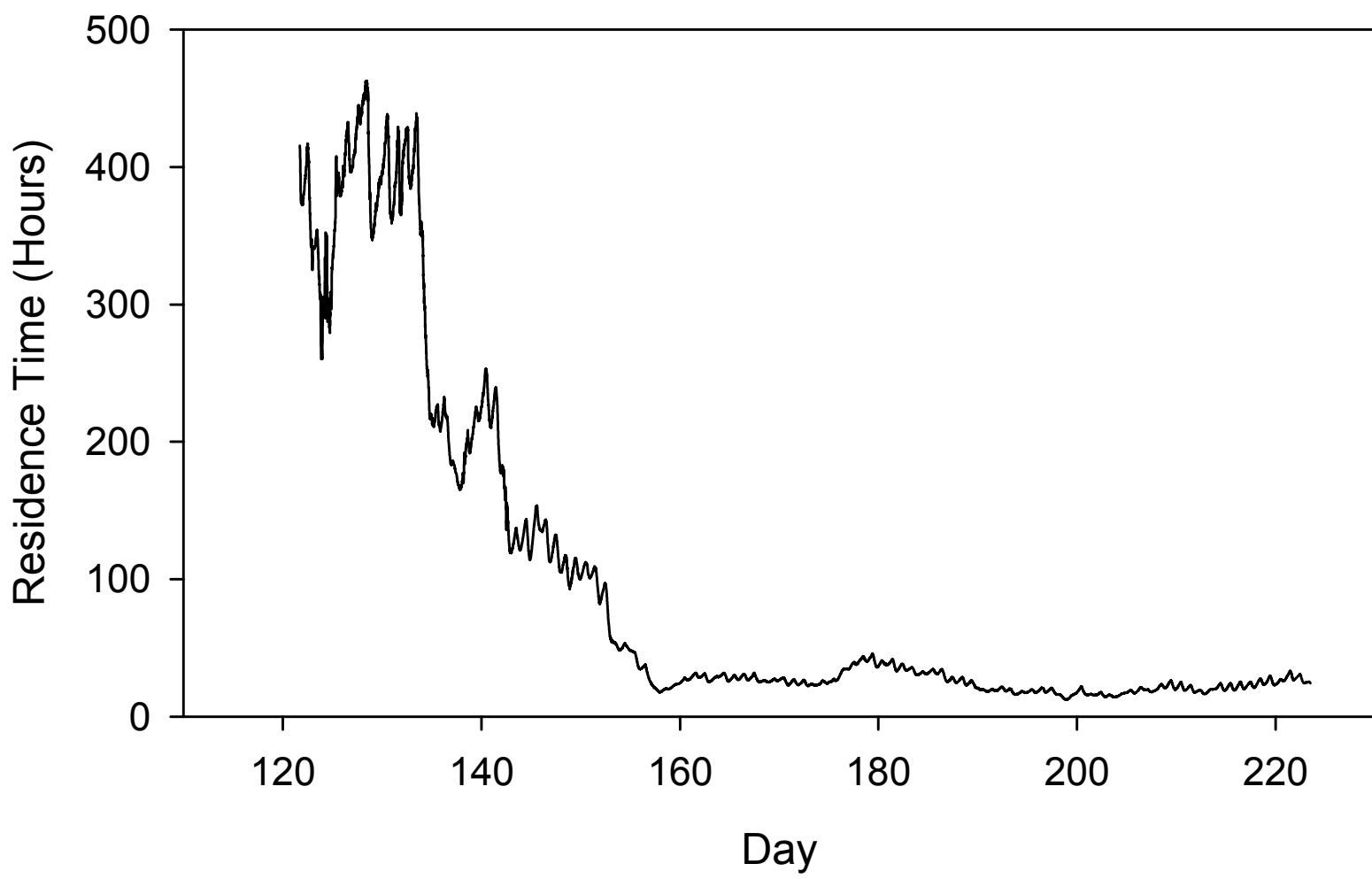
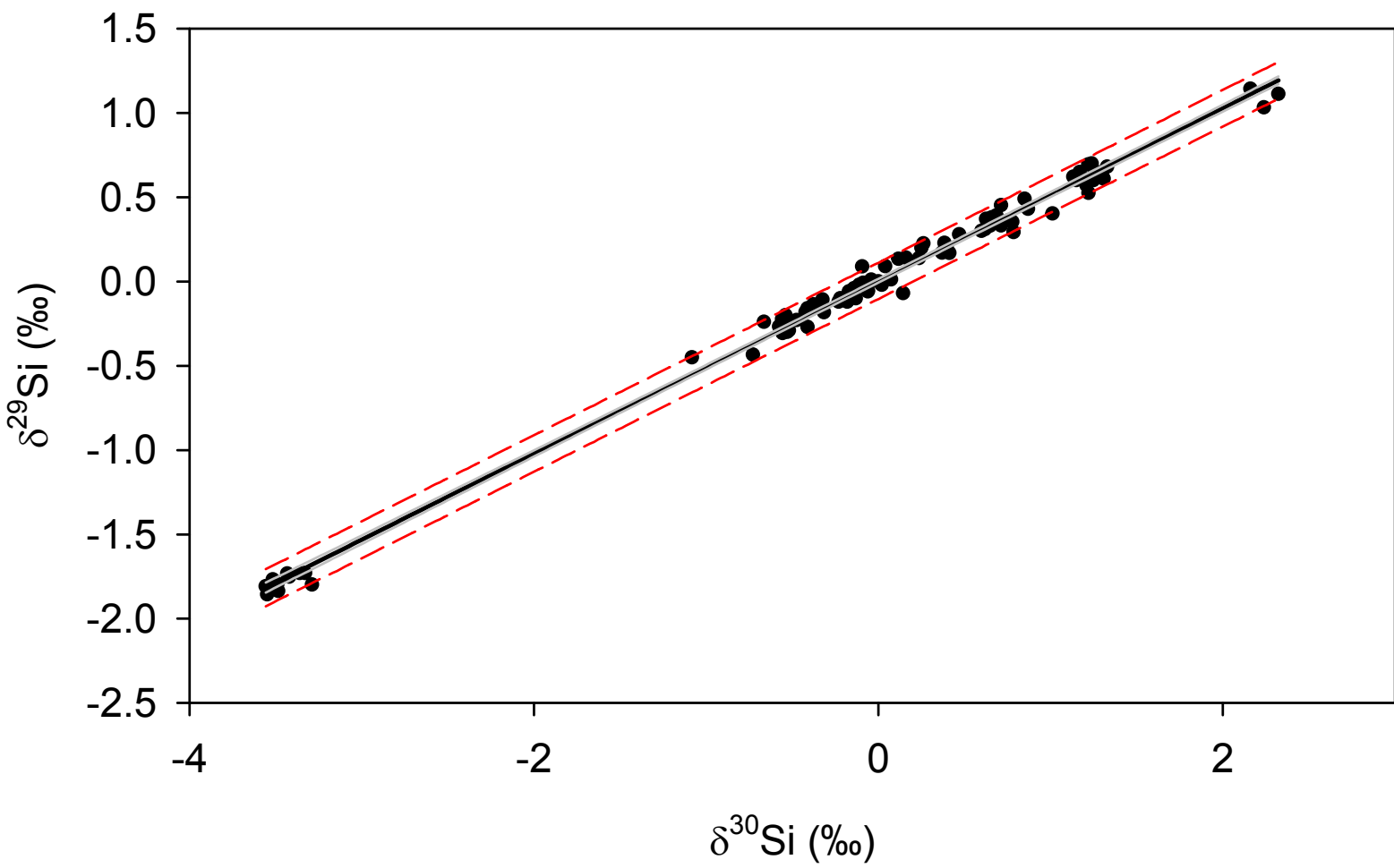
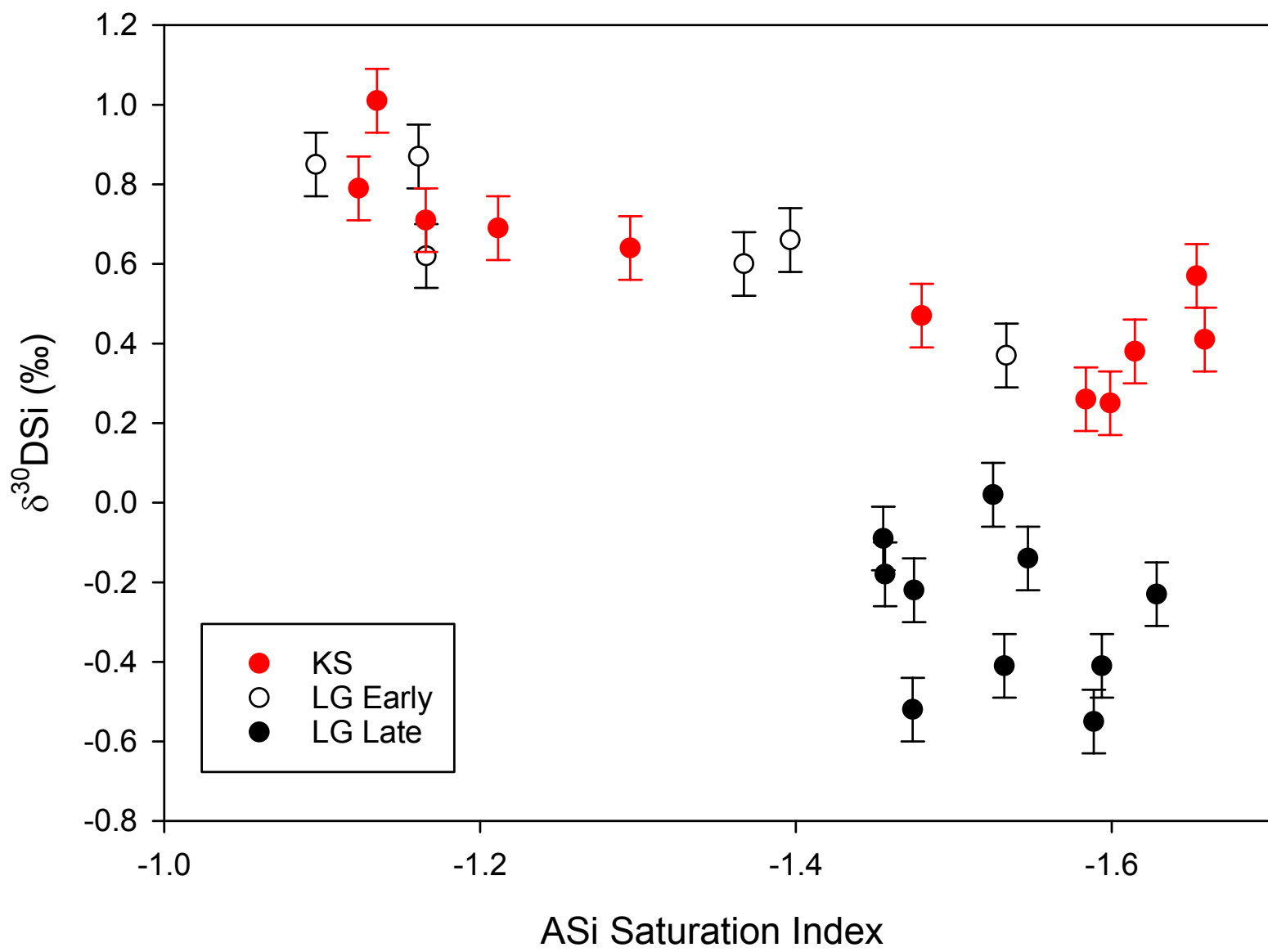


Figure8

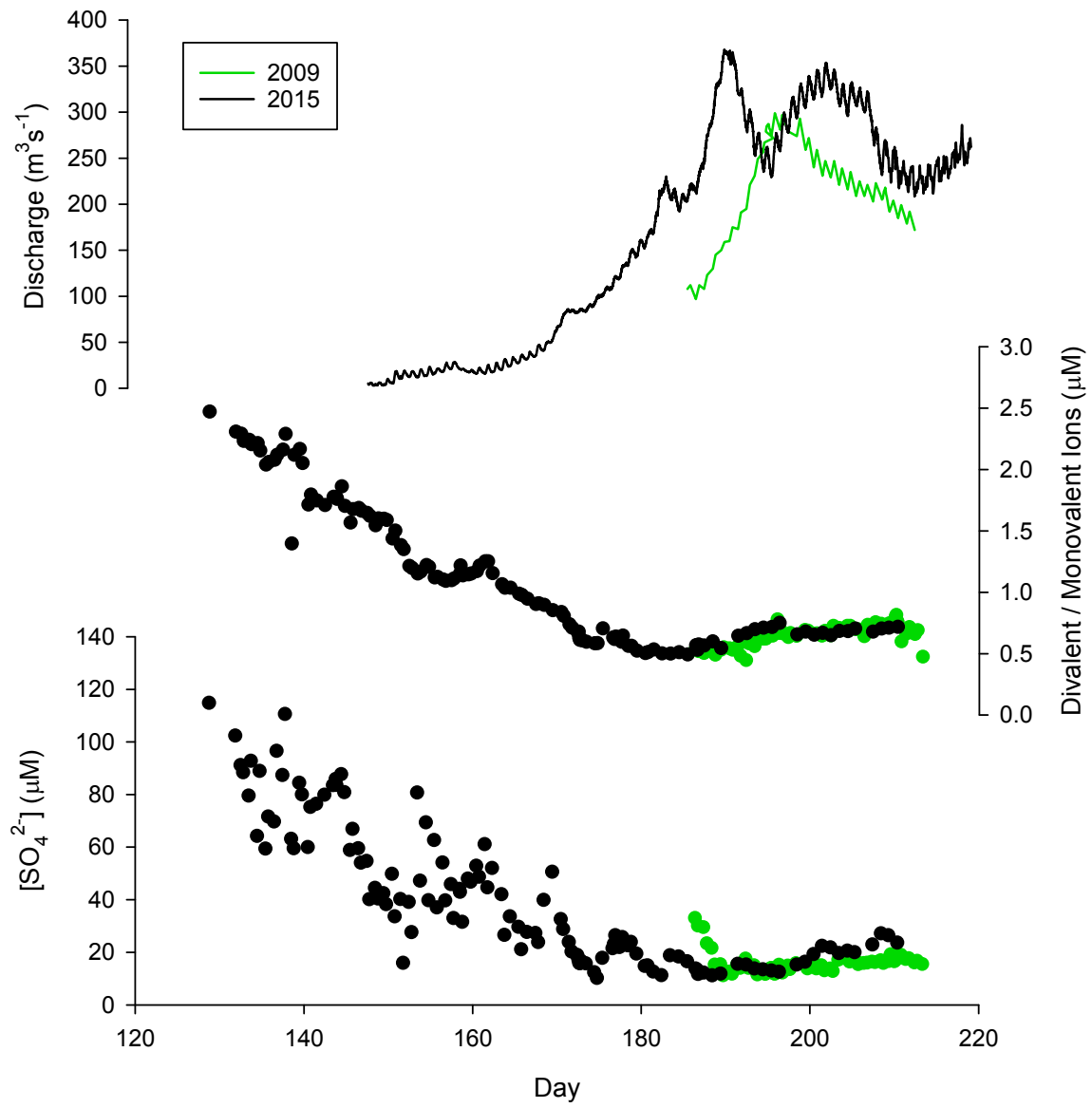


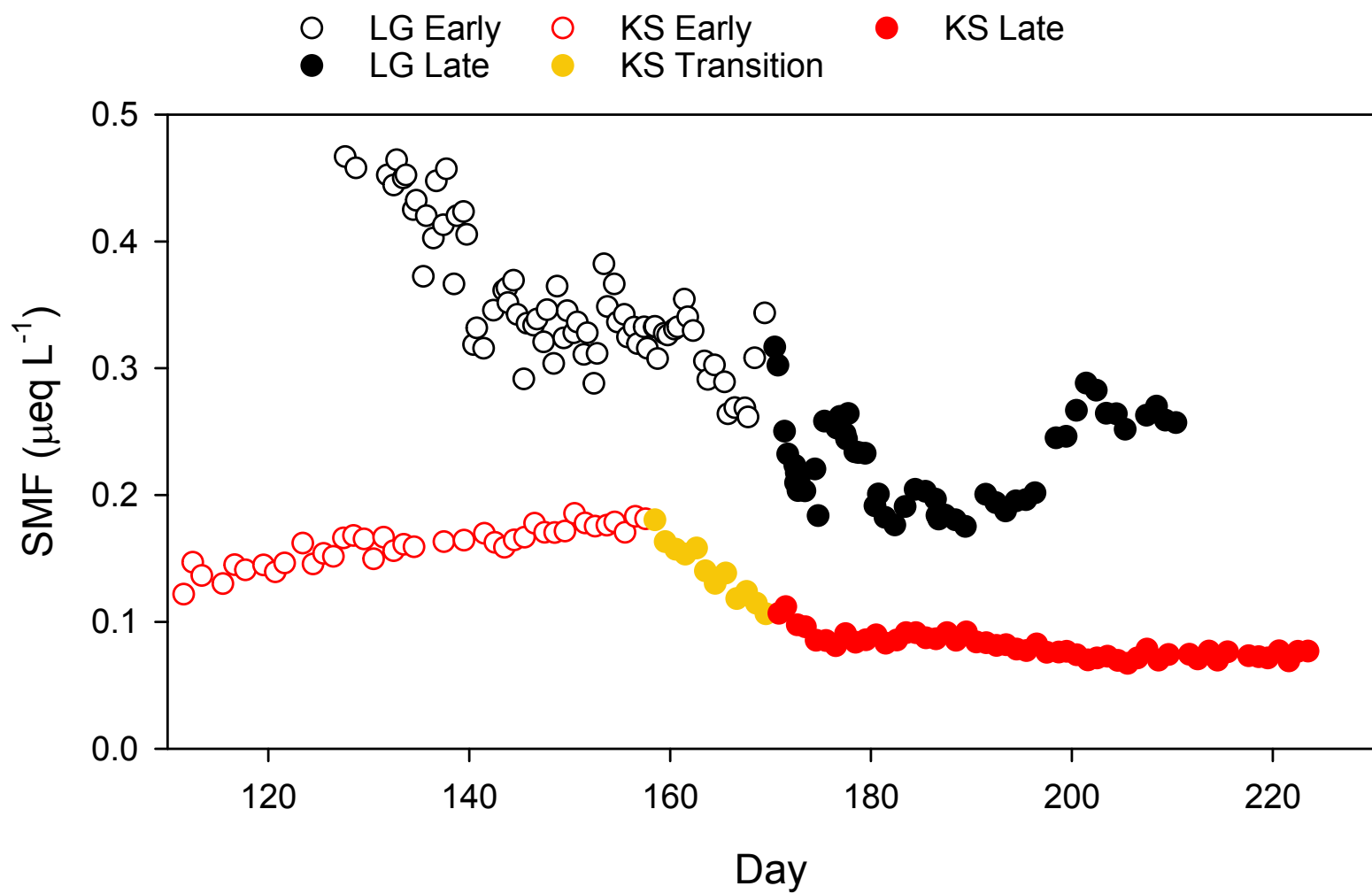


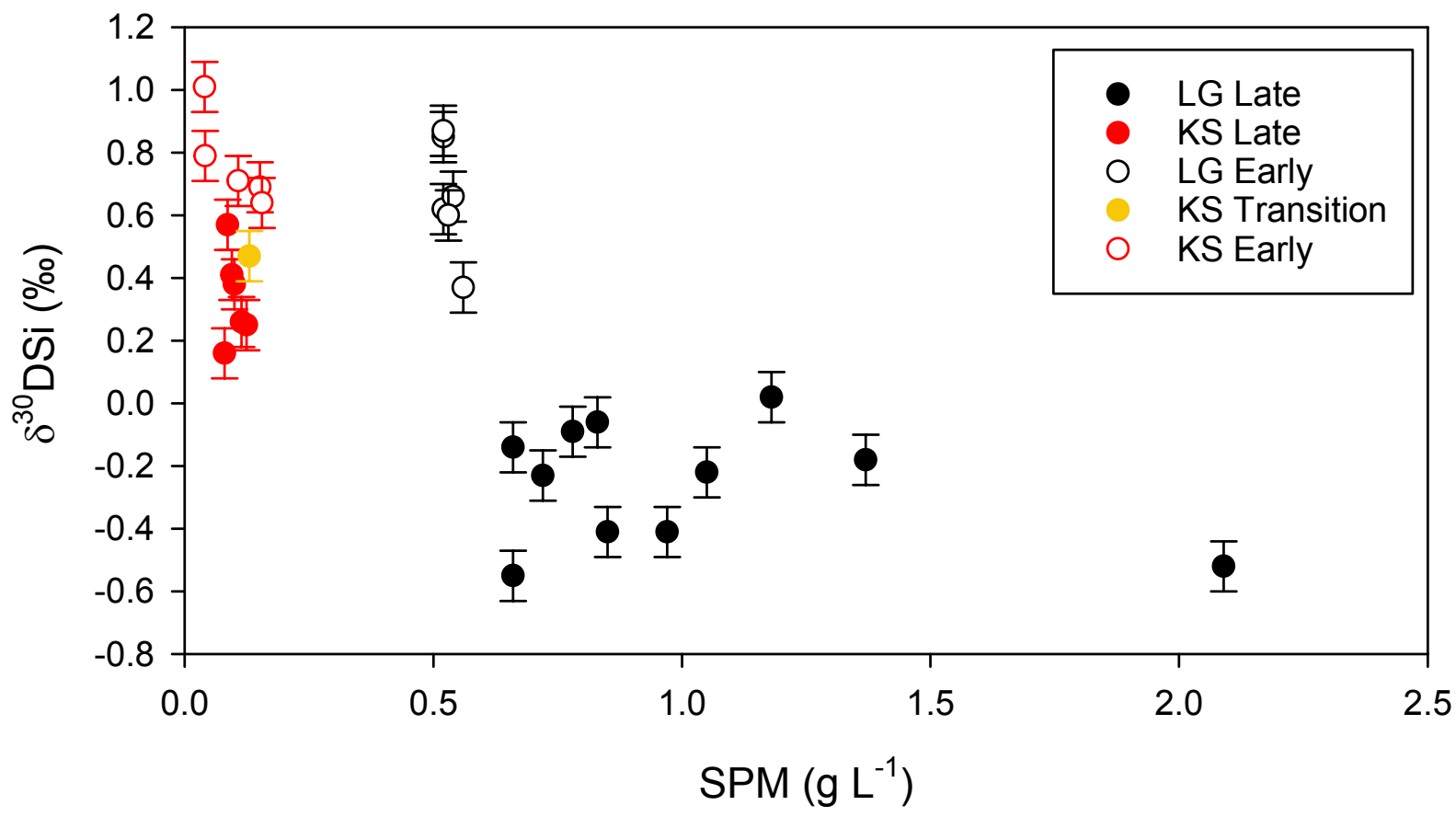




SI Figure4







Equations

[Click here to download Source or Other Companion File: Equations 1-7.doc](#)